SANDIA REPORT

SAND2015-2850
Unlimited Release
Printed April, 2015

An Experimental Study of Shear-Dominated Failure in the 2013 Sandia Fracture Challenge Specimen

Edmundo Corona, Lisa A. Deibler, Benjamin Reedlunn, Mathew D. Ingraham and Shelley Williams

Prepared by
Sandia National Laboratories
Albuquerque, New Mexico 87185 and Livermore, California 94550

Sandia National Laboratories is a multi-program laboratory managed and operated by Sandia Corporation, a wholly owned subsidiary of Lockheed Martin Corporation, for the U.S. Department of Energy's National Nuclear Security Administration under contract DE-AC04-94AL85000.

Sandia National Laboratories

Issued by Sandia National Laboratories, operated for the United States Department of Energy by Sandia Corporation.

Available to DOE and DOE contractors from
U.S. Department of Energy
Office of Scientific and Technical Information
P.O. Box 62
Oak Ridge, TN 37831

Telephone: (865) 576-8401
Facsimile: (865) 576-5728
E-Mail: reports@adonis.osti.gov
Online ordering: http://www.osti.gov/bridge

Available to the public from
U.S. Department of Commerce
National Technical Information Service
5285 Port Royal Rd
Springfield, VA 22161

Telephone: (800) 553-6847
Facsimile: (703) 605-6900
E-Mail: orders@ntis.fedworld.gov
Online ordering: http://www.ntis.gov/help/ordermethods.asp?loc=7-4-0#online

SAND2015-2850
Unlimited Release
Printed April, 2015

An Experimental Study of Shear-Dominated Failure in the 2013 Sandia Fracture Challenge Specimen

Edmundo Corona, Lisa A. Deibler, Benjamin Reedlunn,
Mathew D. Ingraham and Shelley Williams
Sandia National Laboratories
PO Box 5800
Albuquerque, NM 87185

Abstract

This report presents an experimental study motivated by results obtained during the 2013 Sandia Fracture Challenge. The challenge involved A286 steel, shear-dominated compression specimens whose load-deflection response contained a load maximum followed by significant displacement under decreasing load, ending with a catastrophic fracture. Blind numerical simulations deviated from the experiments well before the maximum load and did not predict the failure displacement. A series of new tests were conducted on specimens machined from the original A286 steel stock to learn more about the deformation and failure processes in the specimen and potentially improve future numerical simulations. The study consisted of several uniaxial tension tests to explore anisotropy in the material, and a set of new tests on the compression specimen. In some compression specimen tests, stereo digital image correlation (DIC) was used to measure the surface strain fields local to the region of interest. In others, the compression specimen was loaded to a given displacement prior to failure, unloaded, sectioned, and imaged under the microscope to determine when material damage first appeared and how it spread.

The experiments brought the following observations to light. The tensile tests revealed that the plastic response of the material is anisotropic. DIC during the shear-dominated compression tests showed that all three in-plane surface strain components had maxima in the order of 50% at the maximum load. Sectioning of the specimens revealed no signs of material damage at the point where simulations deviated from the experiments. Cracks and other damage did start to form approximately when the maximum load was reached, and they grew as the load decreased, eventually culminating in catastrophic failure of the specimens.

In addition to the steel specimens, a similar study was carried out for aluminum 7075-T651 specimens. These specimens achieved much lower loads and displacements, and failure occurred very close to the maximum in the load-deflection response. No material damage was observed in these specimens, even when failure was imminent.

In the future, we plan to use these experimental results to improve numerical simulations of the A286 steel experiments, and to improve plasticity and failure models for the Al 7075 stock. The ultimate goal of our efforts is to increase our confidence in the results of numerical simulations of elastic-plastic structural behavior and failure.

Acknowledgment

Many people assisted the authors in carrying out the work presented in this report. The financial support of the WSEAT program provided by David Epp allowed us to conduct the study. Brad Boyce provided the steel plate originally used to manufacture the 2013 Sandia Fracture Challenge specimens in order to manufacture new ones. Jack Heister assisted with the specimen designs and interfacing with the machine shop that manufactured the specimens. Amy Allen acquired the SEM images of the fracture surfaces. Jhana Gorman, Sharlotte Kramer, Artis Jackson and John Laing from the Structural Mechanics Laboratory helped us with various aspects of the project. Everyone's contributions are acknowledged with gratitude.

Contents

Appendix

Figures

Tables

Nomenclature

$E^L_{XX}, E^L_{YY}, E^L_{XY}$	Logarithmic strain components
L_1, L_2	Reference lengths at two locations used to assess symmetry of deformation
P	Compression force
X, Y, Z	Cartesian coordinantes
ΔT	Temperature rise
δ	Relative displacement of platens (average of 4 LVDT signals)
δ_e	Relative displacement of fiducial targets
δ_1, δ_2	Measured deflections used to assess symmetry of deformation
ε	Uniaxial engineering strain
ζ_u, ζ_l	Thin crack length at upper and lower ends of the high deformation region
η_u, η_l	Indentation length at upper and lower ends of the high deformation region
ξ_u, ξ_l	Deformation at upper and lower ends of the high deformation region
σ	Uniaxial engineering stress

1 Introduction

The Sandia Fracture Challenge is a competition in which the participants make blind ductile failure predictions for metal test specimens under a given loading. Information provided to the participants include the specimen geometry, the loading conditions and the results of material tests. The latter have been generally given as engineering stress-strain curves obtained from uniaxial tension tests carried to failure. The results from the challenge specimen tests are not shared with the participants until after they have submitted their blind predictions. Comparisons between predictions and test results are generally based on the load-deflection curves and the geometry of failure. The Sandia Fracture Challenge has been conducted at times with the participation of researchers outside Sandia. The results of one such challenge conducted in 2012 are presented in [1], which states that the objectives were to "benchmark the capabilities for the prediction of deformation and damage evolution associated with ductile tearing in structural metals, including physics models, computational methods, and numerical implementations currently available in the computational fracture community."

In 2013, the fracture challenge was restricted to participants from Sandia and was intended to test the accuracy of predictions for the fracture of a specimen under shear-dominated conditions. Figure 1 shows the geometry of the specimen, which was loaded in compression between two platens, as shown in Fig. 2, using a 22 kip hydraulic testing machine. The specimens were manufactured via wire electric discharge machining (EDM) from a steel A286 flat plate that was annealed and precipitation aged as described in Appendix A. Steel A286 is a high-strength alloy with good corrosion resistance at temperatures up to 1300°F and high ductility in notched sections. This alloy finds use in severe environments such as turbine wheels and blades, afterburner parts and fasteners in jet engines. Nominal yield and tensile strengths at room temperature are in the vicinity of 95 and 145 ksi. The elongation at failure is in the order of 24% with a reduction in area of 45% [2].

Figure 3 shows a comparison of the blind predictions for the load-deflection response of the specimen turned in by the two participating teams against the measurements of the 15 samples tested. The experimental results will be discussed first. Clearly, the load-deflection responses measured in the laboratory are very repeatable. A largely negligible scatter in the points of failure can be seen. The final failure of the specimens occurred in a symmetric manner through two cracks extending through the thickness of the specimen at the locations A and B highlighted in the isometric projection shown in Fig. 1. Figure 4 shows a close-up photograph of one of these locations for a specimen that was unloaded just prior to failure.

We return now to Fig. 3 to discuss the blind predictions. They were based on the geometry and loading specified and on material properties derived from the uniaxial engineering stress-strain (σ-ε) curve shown in Fig. 5. The specimen test section had a nominal length of 1.25 in. and rectangular cross section with width and thickness of 0.250 and 0.125 in. respectively. Fig. B.1 in Appendix B shows a print of the specimen design. The strain was measured using an extensometer with a one-inch gage length. The tests were conducted quasi-statically, at a nominal strain rate of 0.6×10^{-3} 1/s. The specimen was cut from the same plate as the

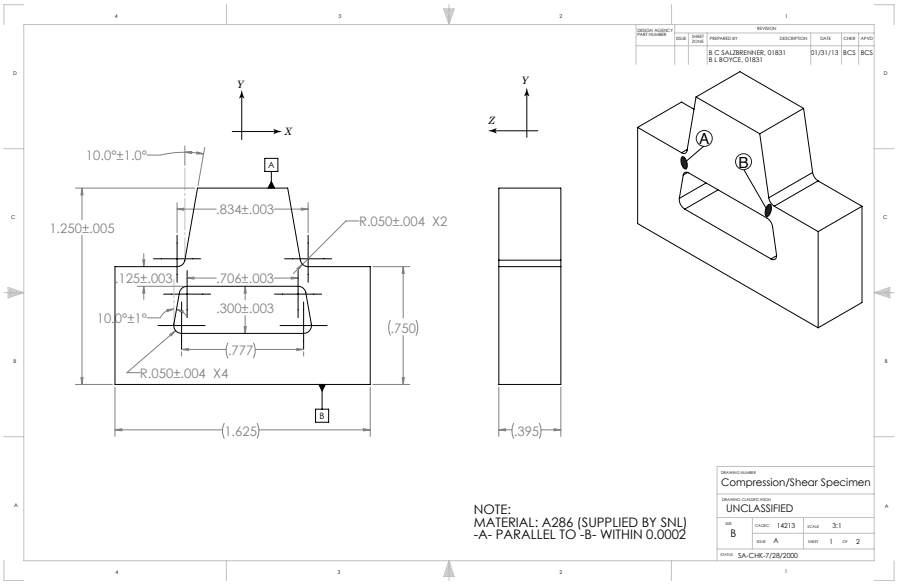

Figure 1: Machine shop schematic of the compression shear specimen. Dimensions are in inches.

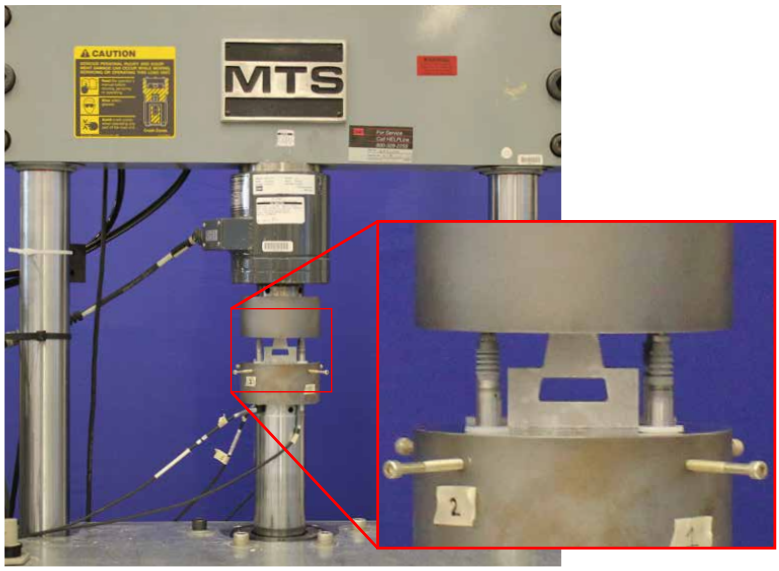

Figure 2: Photograph showing the specimen between the compression platens, which were mounted in a 22 kip frame.

compression specimens and was aligned lengthwise in the Y direction in Fig. 1. The New Mexico (NM) team chose to provide two predictions based on two failure criteria. The red curve in Fig. 3 was obtained using the Multi-Linear Elastic Plastic with Failure model [3] with a Tearing Parameter exponent of 1. The magenta curve was submitted as a lower bound calculated using the same elastic-plastic model but coupled with the equivalent plastic strain failure criterion. Both failure criteria were calibrated to match the failure strain from the uniaxial tension tests. The blue curve is the single prediction submitted by the California

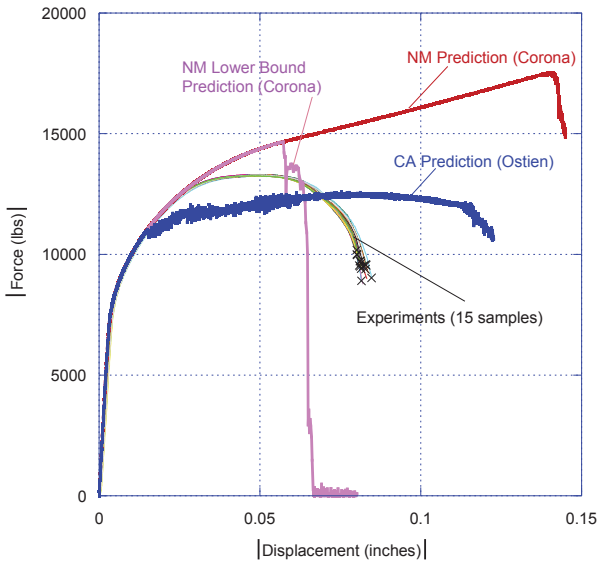

Figure 3: Comparison of blind numerical predictions of the load-deflection response and failure against experimental measurements.

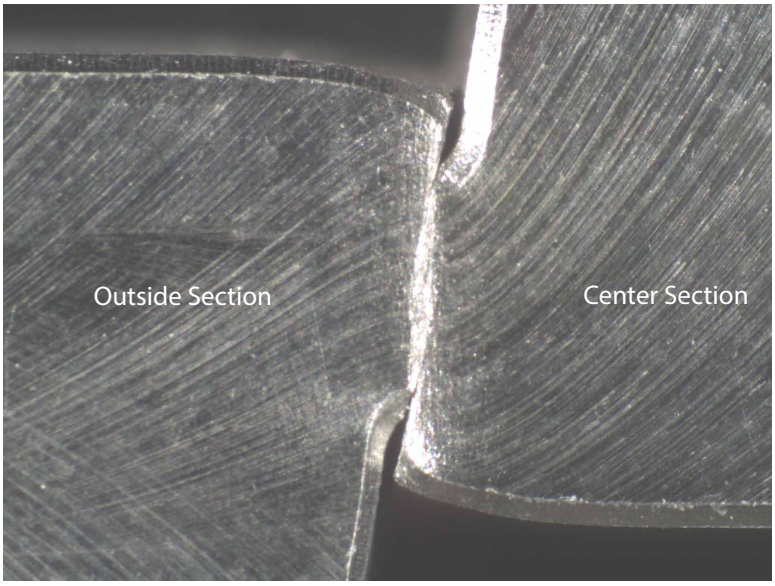

Figure 4: Close-up photograph showing one of the regions where failure occurred in experiment S6. The figure also defines the center and outside regions of the specimen.

(CA) team, calculated using BCJ_MEM, a Gurson-like model, that considered shear in the calculation of the damage. Clearly, both teams missed the load and deflection values at failure. Even more intriguingly, neither team's results followed the measured load-deflection curves at least up to the point of maximum load. The NM predictions overshot the load deflection curves while the CA prediction undershot them.

The comparisons shown in Fig. 3 are the principal motivators for the experimental work

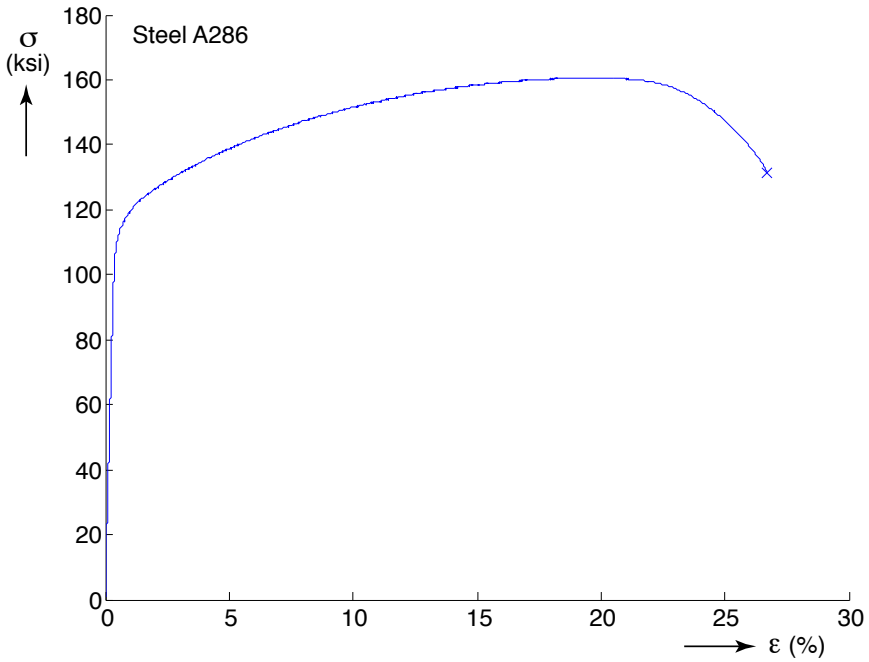

Figure 5: Uniaxial stress-strain curve for steel A286 provided to the participants of the 2013 Sandia Fracture Challenge.

presented here. The objectives are to determine the response of the specimens by careful measurement of the load-deflection response, the strains local to the failure zone and the progression of internal damage that ultimately led to catastrophic fracture. The principal questions that we are trying to answer concern the following:

- What are the likely causes for the deviation of the predicted load-deflection curves from the experimental results observed soon after yielding?
- What damage and fracture mechanisms lead to the catastrophic failure of the specimens, when do they first appear and how do they evolve?

This work attempted to answer these questions by carefully repeating the experiments conducted in 2013. In some experiments, the surface strain fields in the regions with severe deformation were measured using digital image correlation (DIC). In most experiments, the specimens were loaded only part of the way to failure. These specimens were subsequently sectioned and inspected under the microscope to look for the internal damage mechanisms that eventually led to catastrophic failure. This procedure was inspired by the work of Ghahremaninezhad and Ravi-Chandar [4].

Ultimately, it is expected that the conclusions of this work will aid in understanding shear dominated failure and therefore lead to the improvement of numerical models that more accurately capture material behavior under shear dominated loading. If these objectives can

be accomplished, analysts will have better tools to make predictions perhaps involving less uncertainty in situations where shear-dominated ductile failure is a possibility.

While the bulk of the investigation concerns the behavior of A286 steel specimens, specimens with the same geometry were also manufactured from aluminum 7075-T651 plate. These experiments were performed to investigate what the specimen response would be like with a significantly less ductile alloy. This plate stock was chosen because it was previously used in a shear-dominated plate puncture test [5], [6], and the material had been already been characterized through a series of tension tests on smooth and notched specimens.

To parallel the presentation above about the steel specimens, Fig. 6 shows a comparison of numerical predictions against experimental results for the load-deflection response and failure of the specimens. The constitutive model was calibrated using the measured uniaxial stress-strain response shown in Fig. 7. The uniaxial tension test was conducted on a specimen with circular cross-section with test section length and diameter of 1.25 and 0.250 in. respectively. The design of the specimen is shown in Fig. B.2 in Appendix B. The specimen was pulled quasi-statically at a nominal strain rate of 0.16×10^{-3} 1/s. The engineering strain was measured using an extensometer with a one-inch gage length.

The comparison in Fig. 6 clearly shows that the prediction overestimates the load measured in the experiments after yield by about 5%. In this case, however, the deviation of the predictions from the experiments seems to be related to the onset of yield. Note that no significant softening of the load-deflection response occurred in the experiments prior to failure, and that the displacement to failure is significantly less than for the steel specimens. The prediction of failure is based on the Johnson-Cook failure model as calibrated in [6], using the properties labeled "Medium" in that reference. The displacement at failure is predicted reasonably well, but many questions remain regarding failure predictions.

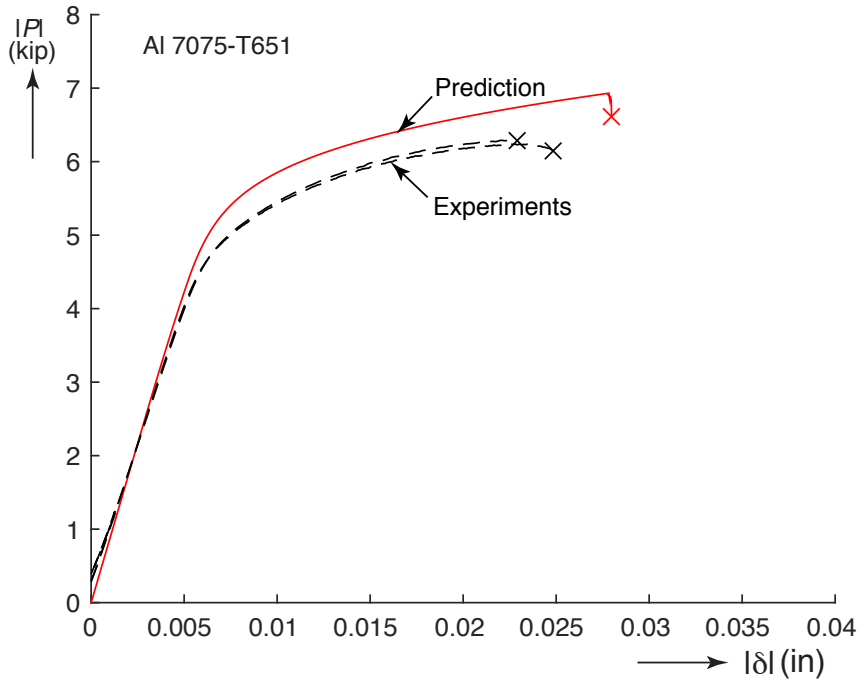

Figure 6: Comparison of numerical predictions of the load-deflection response and failure against experimental measurements for Al 7075-T651 shear dominated compression specimens.

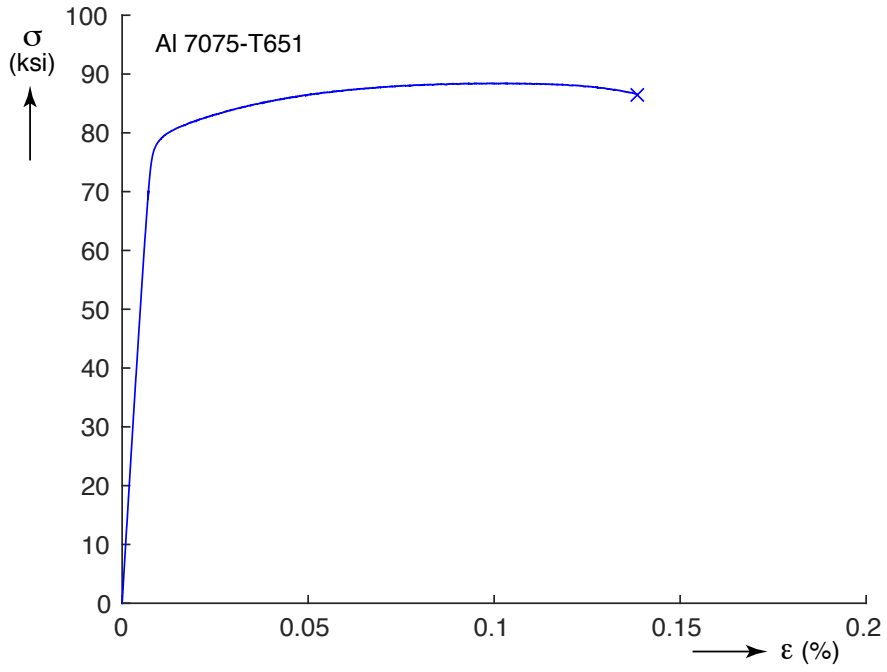

Figure 7: Uniaxial stress-strain curve for an Al 7075-T651 specimen aligned in the rolling direction.

2 Specimen Loading Set-up and Procedure

The specimens were compressed between a pair of four-inch diameter platens mounted on a servo-hydraulic, 22 kip testing frame with closed-loop control (Asset# SNL-55160) as was shown in Fig. 2. The platens were machined from A2 tool steel and hardened to Rockwell C 45 with a #8 mirror surface finish. They were installed in the frame such that the flat surfaces were parallel within 0.001 in. across the diameter in any direction. This was tested with a 0.001 in. shim and Prescale Ultra-low pressure sensing paper (28-85 psi sensitivity). The lower platen has four holes at 90° increments to mount spring-loaded linear variable displacement transformers (LVDTs) with a range of ±0.100 inches as seen in Fig. 8. They were used to monitor the relative motion of the platens and verify that they remained parallel during loading. It was important to center the specimen as well as possible to minimize tilting of the platens during the tests.

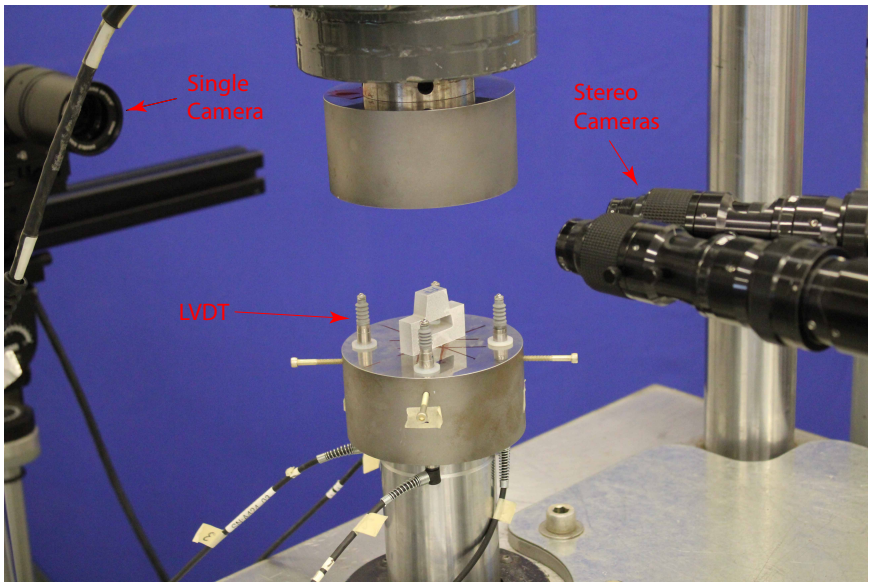

Figure 8: Close-up of the platens showing the three cameras used to acquire the DIC data.

Two Omega type K thermocouples with 0.020 in. probes were also attached to one of the sides of the steel specimens using NTE 303 heat sink compound at the locations indicated by the numbered arrows in Fig. 9. These were used to measure the temperature rise on the surface of the specimen at these points. One thermocouple measured the temperature in the high shear region, while the other was placed near the top of the specimen to serve as reference. Both thermocouples were held in place with cellophane tape.

The testing machine was controlled by an MTS Flextest closed-loop control system. Most experiments were conducted with a constant actuator velocity of 0.001 in/s. Four specimens were loaded with an actuator velocity of 0.0001 in/s. In two cases, the slower rate was used to test whether the load-deflection and failure of the specimens were rate dependent, at least within the loading rates of interest. In the other two cases the specimens were unloaded just prior to failure and required the slower rate to give the operator time to determine the

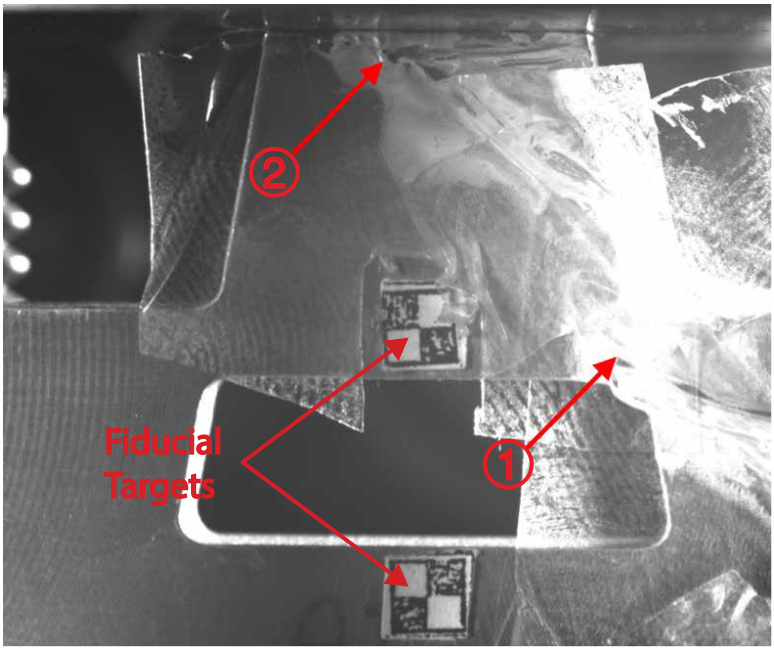

Figure 9: View from the camera tracking the motion of the fiducial targets. The cellophane tape is holding two thermocouples at the locations indicated by the arrows.

unloading point in real time. In all cases, the specimens were first pre-loaded with a 50 lb compressive force prior to the start of the loading ramp. This was done to ensure that the specimen made good contact with the platens and to provide a consistent start point for the next step in each test.

As mentioned in the introduction, one of the principal objectives of the project was to load each specimen to a certain value of displacement and then release the load. Loading multiple specimens in this way and sectioning them allowed observation of the evolution of internal features, such as cracks and voids, with loading. All in all, two steel and two aluminum specimens were compressed to failure while six steel specimens and five aluminum ones were unloaded prior to failure.

Data from the various transducers used in the tests were collected by three different systems. The load and actuator displacement data were collected by the MTS data acquisition system. These two signals were also output to a National Instruments Data Acquisition System that was connected to the camera system and recorded the load and displacement at the time of every digital image. In this way, the load and displacement measurements were synchronized with the digital images. Finally, a separate data acquisition system from HBM collected the load, actuator displacement, LVDT measurements, and thermocouple signals. During post-processing, the load signal was used to synchronize the output from the two latter data acquisition systems.

3 Stereo DIC and Post-Processing

Digital image correlation (DIC) was used to measure the deformation on the front surface of most specimens within the area of the lefthand area of high deformation as shown in Fig. 10. The paint pattern on the specimen was created by first applying a coat of white spray paint to the surface, followed by speckling the surface with black spray paint. This was achieved by spraying the majority of the black paint over the top of the specimens and allowing only some of the paint particles to land on the surface of the specimen. The pattern was made as fine as the test operator's skill would allow in an attempt to increase the resolution of the measurements.

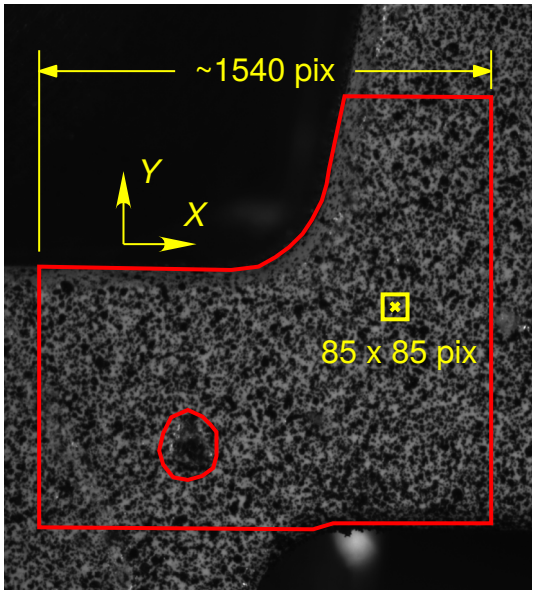

Figure 10: View of the region of interest on the specimen through one of the cameras that acquired image data. The approximate region of interest is outlined in red, and subset size outlined in yellow.

Two cameras, seen to the right in Fig. 8 were used to allow three-dimensional DIC measurements. One of the cameras looked at the specimen straight-on while the other was offset about 15° in a horizontal plane. A third camera, seen to the left of the figure, was placed behind the test system in order to measure the relative in-plane motion of a pair of fiducial targets placed on the back of the specimen as shown in Fig. 9. They had black and white squares with lengths of 0.05 in. on the side, for a total fiducial size of 0.1 in. The cameras were Pt. Grey Research Grasshoppers2 (GRAS-50S5M-C), each with a 2048×2448 pixel array of square 3.45 μm pixels. They were fitted with Navitar lens sets comprised of 6.5×12 mm lenses mounted on 0.67X extension tubes and c-mount adapters[1]. The specimens were illuminated using large panel LEDs[2].

Prior to the experiments, the DIC stereo system was calibrated using a 9×9 calibration

[1]Navitar part numbers 1-60135A, 1-6020, 1-6010 respectively
[2]Bescor LED 500D.

Table 1: Reference coordinates corresponding to the dimensions in Fig. 11

Experiment ID	G, in. (pix)	B_e, in.	L_e, in.
S7	0.3000 (573.6)	0.106	0.558
A6	0.2987 (576.8)	0.117	0.528

grid with 0.89 mm spacing. DIC images were taken at different rates depending on the displacement rate set in the loading program. For the faster rate tests (0.001 in/s) images were taken at a rate of 2.5 Hz. For the slower tests (0.0001 in/s) images were taken at 0.5 Hz. The image capture rates for both the DIC cameras and the fiducial tracking camera were the same, and the images were captured at the same time.

After each experiment, the DIC images were analyzed using the commercially available Vic-3D 2012 software [7] across the region of interest shown in Fig. 10. We utilized a 85×85 pixel subset, an analysis grid with 10×10 pixel spacing, and Vic-3D's default cross correlation function of the normalized sum of squared differences [8]. The subset size used is large compared to those with a more typical size of 21×21 pixels, but we found it was necessary to avoid de-correlation as the specimen deformed. In future work, we may attempt to reduce the speckle size, which would allow us to reduce the subset size. The deformed images were compared against the undeformed reference image to calculate the displacements for the aluminum specimens (referential correlation). Both a referential and an incremental approach (where the preceding image is used as reference) were used for the steel specimens. They gave the same results up to maximum load. The results of the incremental approach are shown in this report.

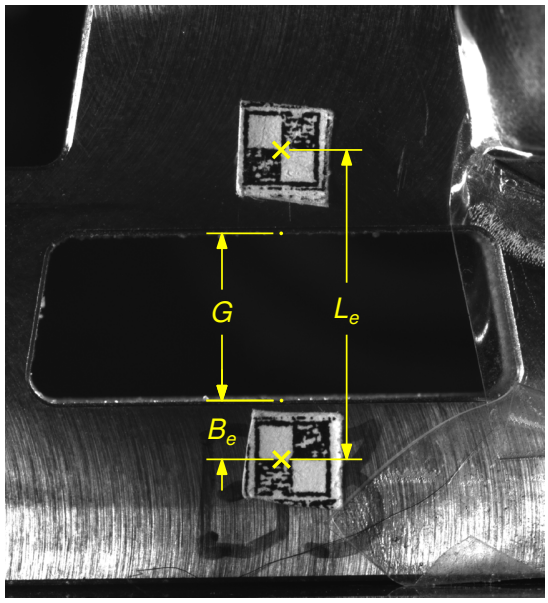

Figure 11: Dimensions locating the fiducial analysis points on specimen S7.

Vic-3D used the displacement fields found during the correlation to calculate the surface

strains at each analysis grid point. The strains were then filtered using a truncated Gaussian filter over a 91 pixel diameter circle with a weight of 1 at the center point and a weight of 0.1 at the circle edge. The strain components from DIC analysis were reported with respect to the referential Cartesian coordinate system (X, Y, Z) shown in Fig. 10. We chose to report the log strain $\boldsymbol{E}^L = \ln \boldsymbol{U}$, where $\boldsymbol{U}$ is the right stretch tensor, because this measure is frequently used in finite strain plasticity. For the reader unaccustomed to thinking about log shear strain, we note that it linearizes to the infinitesimal shear strain, but it does not have a clear physical interpretation for finite shear strains. In fact, one typically calculates $\ln \boldsymbol{U}$ by transforming $\boldsymbol{U}$ from the reference frame into the principal frame (where there is no shear), taking the natural logarithm of the principal stretches, and transforming the components back into the reference frame.

The fiducial images were acquired using the same type of camera with a 55 mm fixed focal length Edmund Optics lens. The images were analyzed using the commercially available Vic-2D 2009 software [9]. This two-dimensional measurement method assumes that the out-of-plane movement of the specimen was negligible. The position of each fiducial was tracked by placing a region of interest on the fiducial. Subset sizes of 199×199 pixels and 153×153 pixels were used in experiment S7 and experiment A6, respectively. The deformations are virtually affine in the vicinity of the fiducials, so large subset sizes are preferable because they lead to a better correlation. Figure 11 shows the fiducial analysis locations for specimen S7, and the values of the dimensions shown for specimens S7 and A6 are listed in Table 1. The conversion from pixels to inches was determined by measuring height of the gap G using a Zeiss Contura optical measuring system, and dividing this by the height of the gap in pixels.

4 Results from Steel A286 Specimens

4.1 Fracture Surface Imaging

This section presents post-failure images of the fracture surfaces obtained using a scanning electron microscope (SEM) on the remains of a 2013 Fracture Challenge Specimen. It was mentioned in Section 1 that the deformation and failure of the specimens seemed to occur in a symmetric manner. One can expect, however, that the specimen failed first at either location A or B in Fig. 1. The fact that some asymmetry occured is clearly seen by examining the fracture surfaces. Figures 12 (a) and (b) show SEM images of the fracture surfaces on both sides of the outside section (see Fig. 4 to identify the 'outside section') of one of the specimens tested to failure (note that the surfaces imaged are not mating surfaces). Clear differences can be seen. Whereas the right side[3] surface in Fig. 12 (a) shows regions with starkly different textures, the left side surface in Fig. 12 (b) shows seemingly less differentiated regions. Examination of all 14 fractured specimens showed that all displayed the same asymmetry of the fracture surfaces.

Figure 13 shows the regions marked in Fig. 12 at higher magnification. Looking first at Fig. 12 (a), magnification of the surface with rough texture at A shows a sub-structure with many equiaxed dimples in each of the flake-like formations that give this region a rough texture. Equiaxed dimples such as these are indicative of tensile failure [10]. The regions labeled A′ and A″ also show similar fracture features. The region at B, which extends across the top of the sample fracture surface, shows a relatively smooth, or "smeared" surface with no evidence of dimples. It is possible that this surface was smeared by the fracturing process or perhaps by rubbing after it fractured. In contrast, the also smooth-looking surface at C exhibits evidence of dimples that have a preferential orientation. Inspection of the mating fracture surface confirmed dimples pointing the opposite direction, suggesting a shear type of failure. Looking next at Fig. 12 (b), D corresponds to the same (Y, Z) coordinates as the rough surface A″ in Fig. 12 (a), except it is on the right side of the outer section. The smooth surface at D shows a texture with dimples that are also elongated, thus suggesting shear dominated fracturing. Within the middle section of the specimen, at E, a rougher texture with some flake-like features and a reasonably equiaxed dimpled substructure can be observed. This seems similar to region A in Fig. 12 (a), but with smaller flake-like formations. Region F displays very similar features as region C. Finally, the region that corresponds to the same (Y, Z) coordinates as location B in Fig. 12 (a) shows essentially the same smeared texture. In summary, although the general appearance of the two surfaces in Fig. 12 is different, they have the following in common:

- The smeared region along the top of the fracture surface.
- The rougher sections with equiaxed dimples in the center area of the fracture surfaces.

[3]Right and left sides are defined to be as seen when facing the painted surface of the specimen, as shown in Fig. 2.

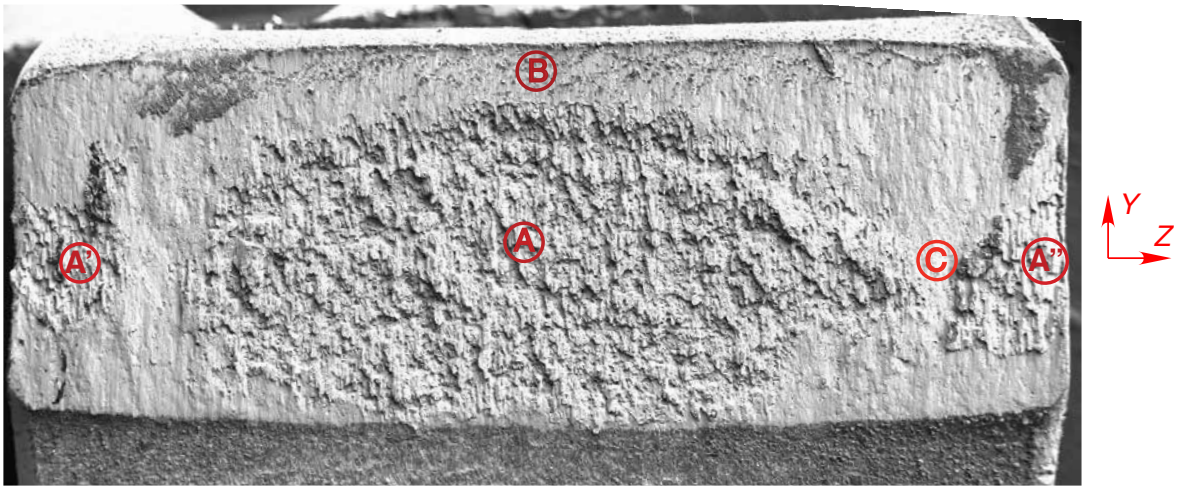

(a)

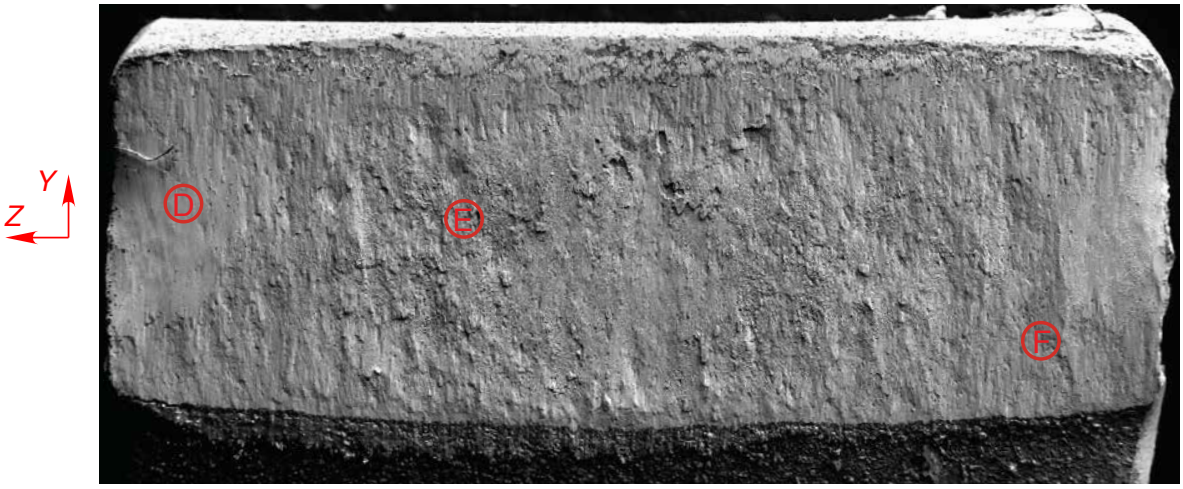

(b)

Figure 12: Typical fracture surfaces seen in the tests. The surfaces shown are for specimen S8. (a) Right side, outside section and (b) left side, outside section. Note that these are not mating surfaces.

- The section around the center and away from the vertical edges that contains elongated dimples suggesting shear failure.

- The sections near the vertical edges that have similar overall shapes. Here, however, in one case the fracture surface is rough, while in the other it is rather smooth with elongated dimples.

The questions that arise are: what are the actual reasons that the surfaces are different? Is the observed asymmetry expressed just at the moment of failure, or does it develop gradually during the test? What is the actual sequence of events at the time of catastrophic failure? Although the instrumentation used in the tests did not allow for examination of the

actual events at the instant of failure, the extent of symmetry in the deformation and of the damage prior to failure will be addressed in the metallographic results portion of Section 4.3.

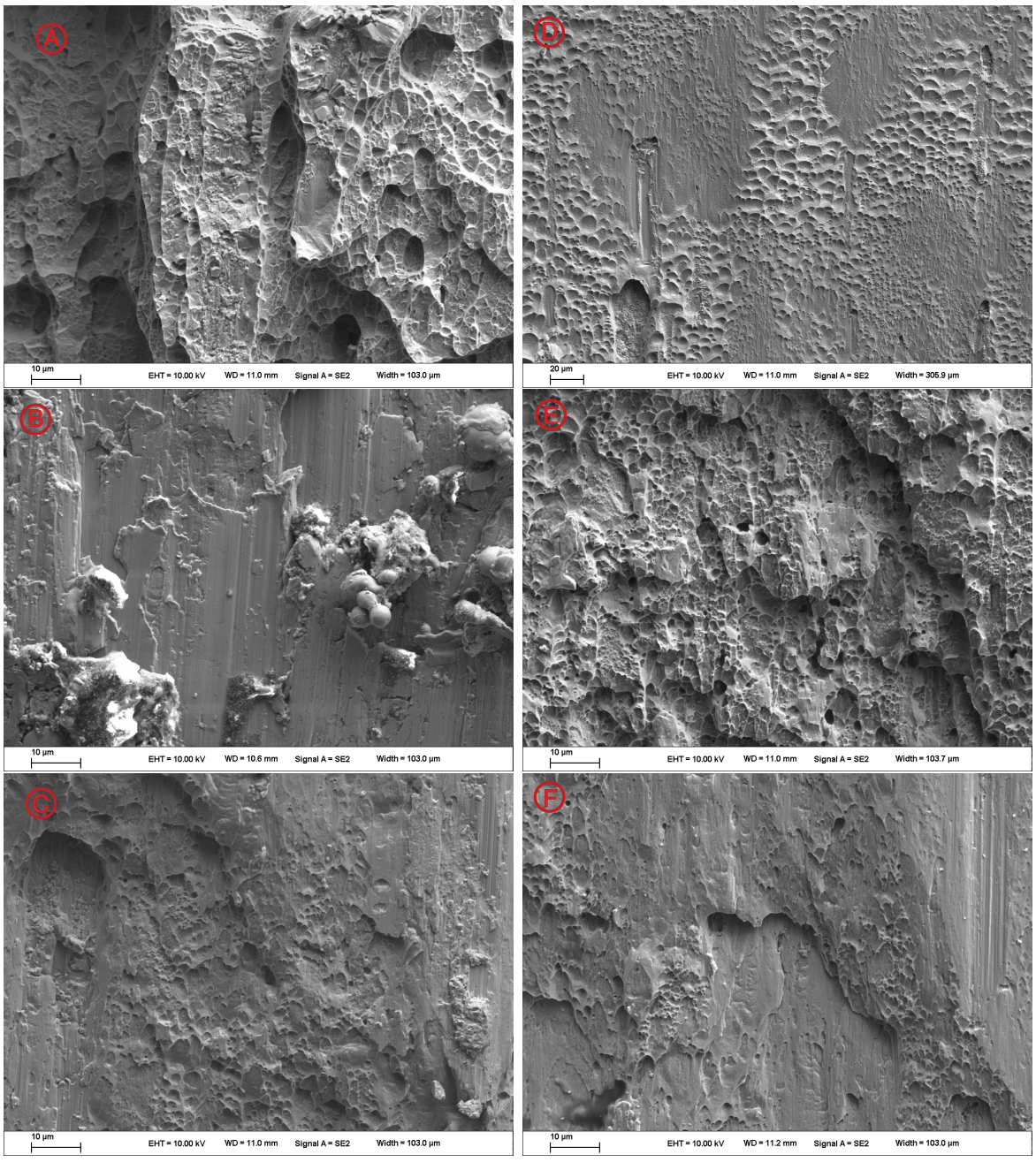

Figure 13: Photographs of regions marked in Fig. 12.

4.2 Material Uniaxial Stress-Strain Response

A part of the work conducted involved a moderately more extensive investigation of the response of the material under uniaxial tension, with the objective of trying to identify

whether yield anisotropy was present in the material. The geometry of the specimens was also as given in Appendix B, Fig. B.1. The strain was measured using an extensometer of one inch gage length. The nominal strain rate was 0.7×10^{-3} 1/s. The results are displayed in Fig. 14. The figure shows stress-strain curves of specimens machined so their axes were aligned with either the X or Y directions defined in Fig. 1 plus another specimen aligned at 45° to these directions. Clearly, anisotropy in both plastic deformation and strain to failure are present. In particular, note that the 45° specimen had lower flow stress. This fact points to a lower in-plane shear flow stress than would have been predicted by the von-Mises based model, paired with the X curve, as was assumed in the blind predictions by the NM team. The effect of material anisotropy in the predictions will be pursued in the near future.

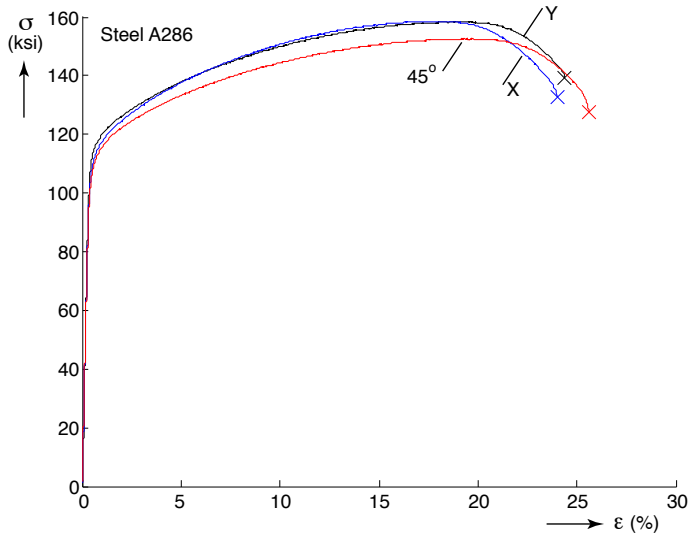

Figure 14: Uniaxial engineering stress-strain curves for steel A286 coupons cut along three directions.

4.3 Shear-Dominated Compression Specimen Investigation

Figure 15 shows load vs. compressive displacement (P-δ) plots for all tests conducted on the steel A286 specimens. The label for each curve corresponds to the experiment number[4]. Most specimens were loaded with a nominal platen speed of 0.001 in/s, as was done in 2013 tests for the fracture challenge competition. The loading rate for two specimens, S6 and S8, however, was 0.0001 in/min. Specimens S7 and S8 were compressed to failure. All others were unloaded at various values of displacement as shown in the figure. The labels Ⓐ through Ⓕ in the figure correspond to the final displacements of these specimens.

Experiment S8 was loaded to failure with a lower strain rate in order to assess if any rate

[4]The experiment numbers have been re-labeled for ease of reading. Appendix C lists the equivalence between the labels used in this report and the original experiment numbers, which are also used in the the test data archived.

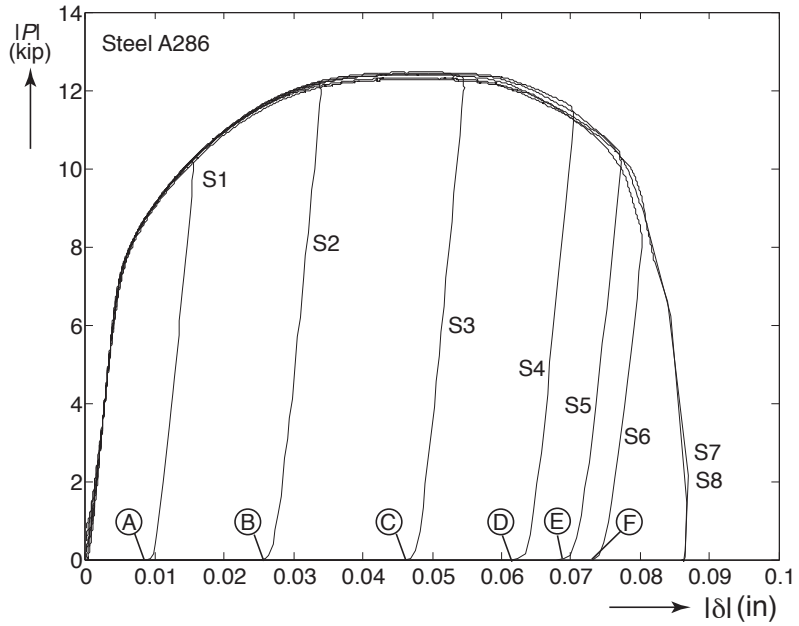

Figure 15: Load vs. platen relative displacement (average of four LVDT signals) for all tests conducted on Steel A286. The extent of compression is clearly seen for all specimens tested.

dependence of the material would be apparent during the study. As can be seen in Fig. 15 the responses of tests S7 and S8 are virtually identical, thus indicating little rate dependence for the platen speeds considered. Figure 16 shows the temperature increase on the surface of the region of intense deformation measured by thermocouple 1 in test S7. Clearly the temperature rise was very modest, in the order of 7 °F. Although output of thermocouple 2 was not recorded in test S7, we can report that the temperature remained virtually constant at that location in all the other tests. Similar measurements for the slower test S8 showed temperature fluctuations in the order of fractions of a °F through the complete loading history at both thermocouple locations.

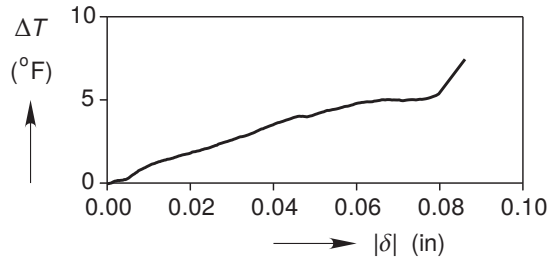

Figure 16: Temperature increase on the surface of a high deformation region in test S7.

The platen displacement δ is compared against the relative displacement of the fiducials δ_e in Fig. 17, and the difference is small. This difference provides some quantification of the deformation near the interfaces between the specimen and the platens. As expected,

the relative displacement of the fiducials is slightly smaller than that of the platens. For the purposes of this report, the platen displacement measurement is sufficient, but future modeling efforts may wish to use the fiducial displacement for a more accurate comparison between experimental measurements and model predictions.

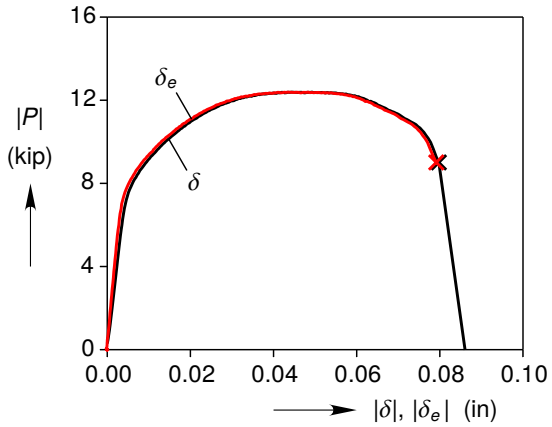

Figure 17: A comparison of the platen displacement δ against the relative displacement of the fiducials δ_e in test S7.

The asymmetry of the fracture surfaces on the left and right sides of the specimen presented in Fig. 12 prompted an investigation of the symmetry of the global deformation of the specimen. This investigation was carried out by tracking the changes in the lengths L_1 and L_2 as defined in Fig. 18. The measurements were conducted on the images acquired in test *S7* by tracking the relative motion of the top and bottom edges of the hole in the specimen at the two points indicated.

The results are shown in Fig. 19. They demonstrate that the global deformation of the specimen had a high degree of symmetry. Hence, it appears likely that the asymmetry in the fracture surfaces developed right about at the point of catastrophic failure. Further evidence of the symmetry of the development of damage in the specimen will be presented in section 4.3.

DIC Analysis Results

Figure 20(a) shows the P-δ response for test S7 with four points marked on the curve. The displacement at points ① through ③ points correspond, as closely as possible, to the maximum displacements in experiments S1, S2, and S3. The four points also correspond to the DIC strain field measurements shown in Fig. 20(b). Each of the three columns correspond to measurements of the strain components E^L_{XX}, E^L_{YY} and E^L_{XY} while the rows correspond to the points marked in Fig. 20(a).

Before examining the strain field images in detail, it is important to note that digital image correlation always performs a certain degree of smoothing during the correlation, and further smoothing is typically performed to calculate the strains [8]. In some applications

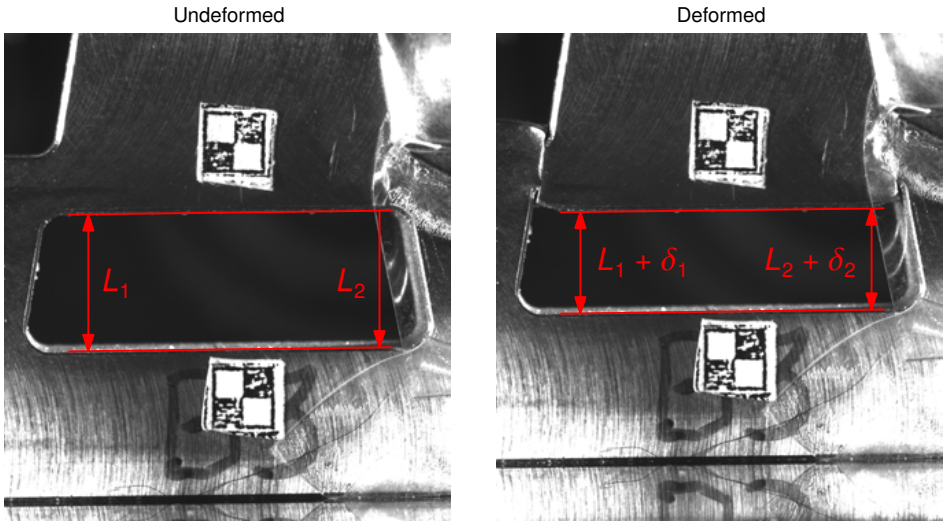

Figure 18: Photographs showing the measurements made to investigate the parallelism of deformation of the right and left sides of specimen S7.

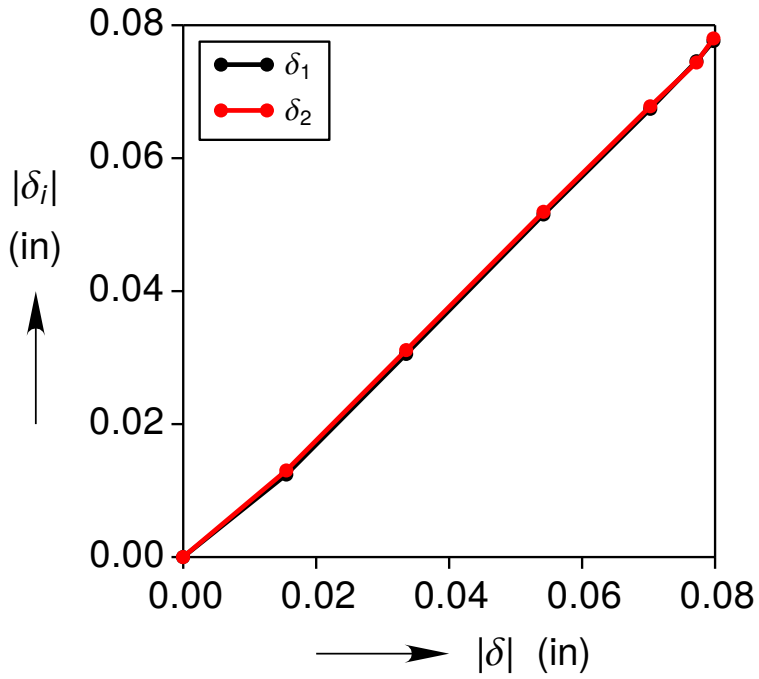

Figure 19: Measurement of the displacements δ_1 and δ_2 as functions of the relative platen displacement δ in specimen S7 showing that the global deformation of the specimen was essentially symmetric.

of DIC, the smoothing is negligible because the areas of interest do not include high strain gradients, but here we have a significant amount of strain localization preceding failure. Thus, one should consider the magnitude of each strain field in Fig. 20(b) as a lower bound on the actual magnitude of the actual strain field.

The strain fields show that the specimen design worked well in concentrating the deformation of the specimen in a narrow zone from the beginning of the test. All three strain components develop gradually prior to the maximum load. The shear component grows somewhat faster than the other two, but all of them are in the same order of magnitude. At the time of the load maximum (point ③) E^L_{XY} has a maximum value in the order of 50% over a fairly long vertical region at the center of the high deformation region. This strain component decreases near the edge of the specimen where no shear strain would be expected. E^L_{XX} and E^L_{YY} show maximum values in the order of 40%, but with the higher values tending towards the upper and lower edges of the high deformation region. In the central part of this region, where the shear component is highest, the normal strains are in the order of 30-40%. Also note that the geometry of the shoulder between the center and side regions of the specimen, which was originally a smooth radius sharpened considerably by the time the maximum load was achieved. This will be discussed in more detail in Section 4.3.

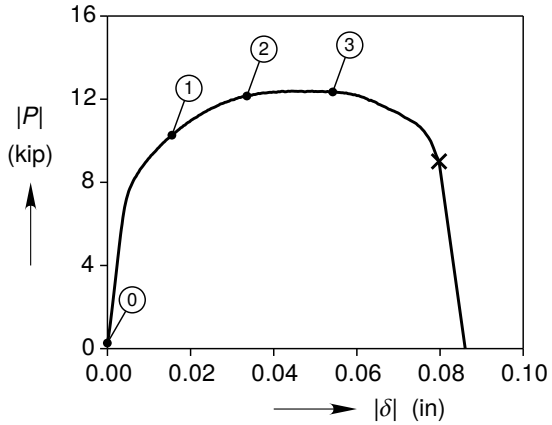

(a)

Figure 20: DIC results for experiment S7. (a) Load-deflection response. The numbers in the balloons correspond to the images shown in Fig. 20 (b).

Strain field measurements were collected beyond the maximum load, but they are not shown because we later discovered that a surface crack or very steep strain gradients may have contaminated the results. In lieu of those results, Fig. 21 shows a mechanical response curve and a sequence of photographs taken at the same location on specimen S6. The first four circled numbers along the P-δ curve match those in Fig. 20(a) and the next three circled numbers correspond, as close as possible, to the maximum displacement experienced by specimens S4, S5, and S6. In test S6, the front face of the specimen was not painted and displayed machining marks left over from the manufacturing process. One of the lines has been highlighted in red. Up to point ③, corresponding to the maximum load, the line deformed into a smooth curve that could be traced. After the maximum load, however,

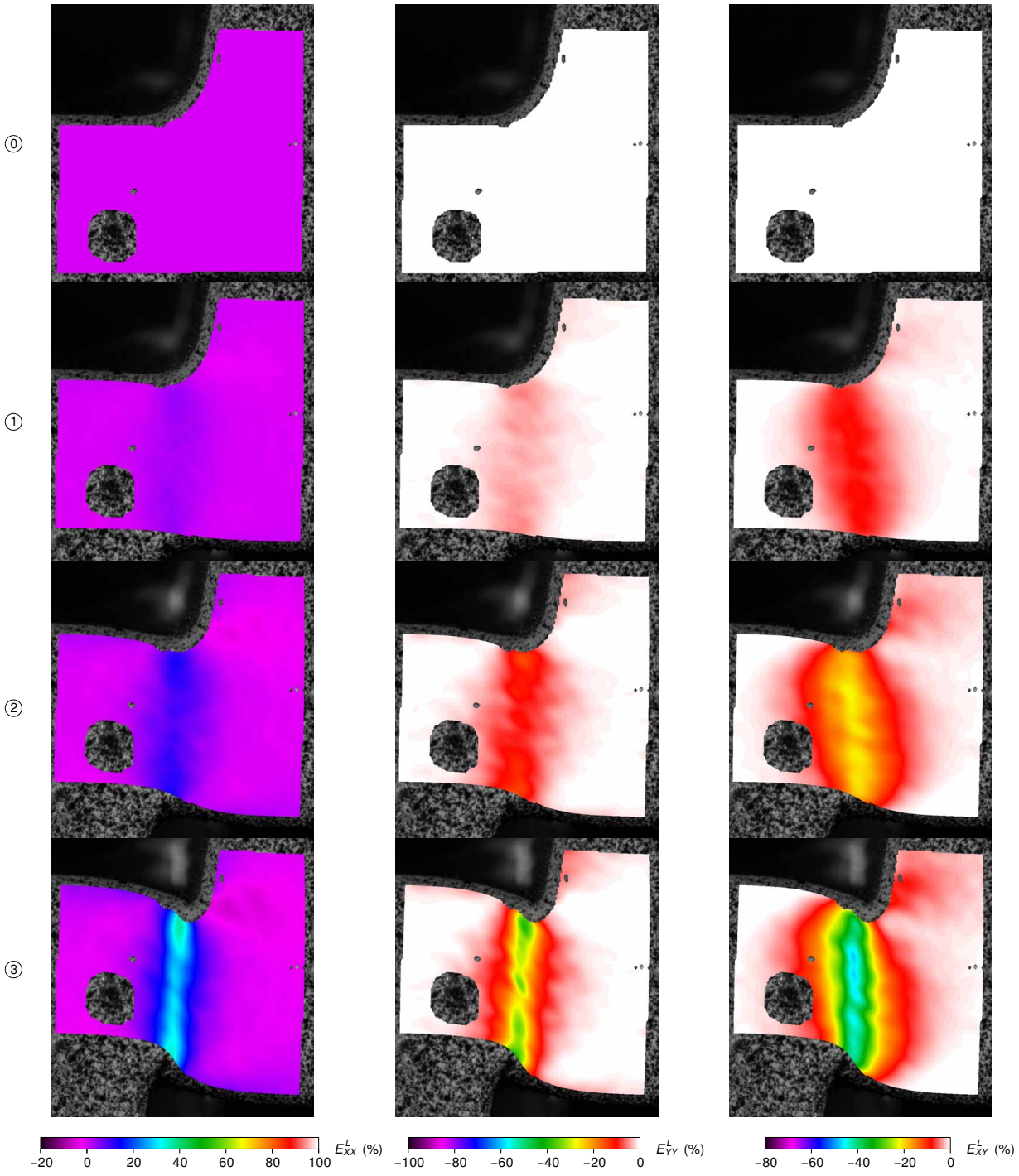

(b)

Figure 20: **(continued)** (b) Surface logarithmic strain components from the beginning of loading until the point of maximum load. X and Y represent the horizontal and vertical directions, respectively.

it became increasingly difficult to trace the line in the region of high deformation, and it appears to be discontinuous, likely indicating that either a region with extremely high strain or a crack had developed. If it was a crack, then it would be of interest to determine its depth into the specimen. The subject of the fracture process that eventually leads to failure of the specimen will be treated in the next section.

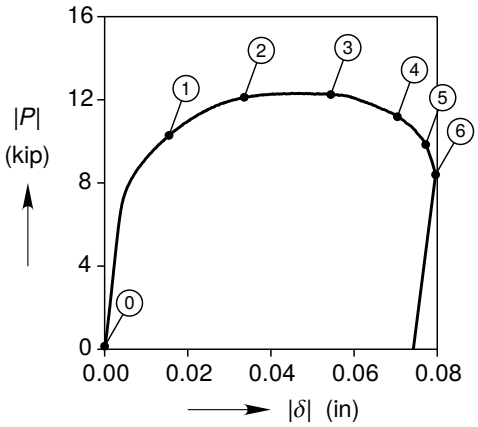

(a)

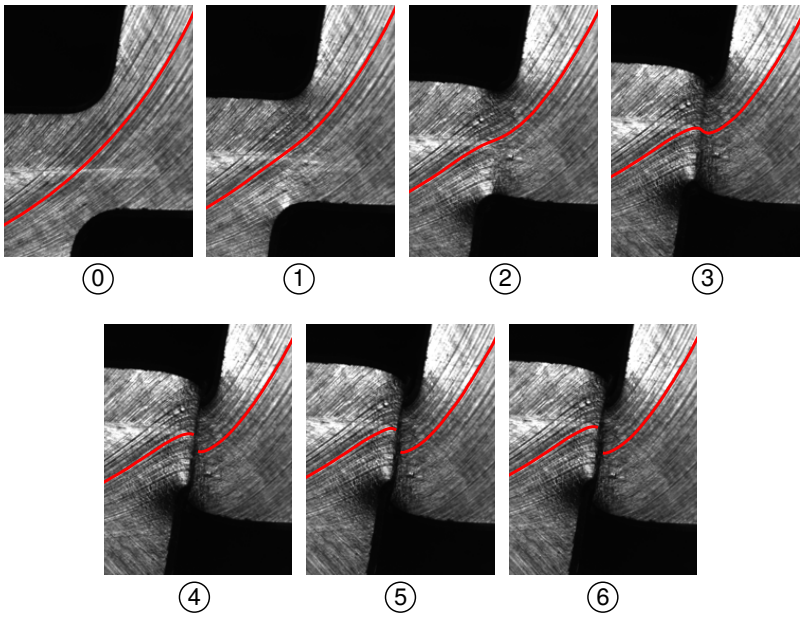

(b)

Figure 21: Mechanical response and surface images for experiment S6. (a) Load-deflection response and (b) machined surface images. The circled numbers in (a) correspond to the images shown in (b).

Metallography Analysis

Specimen Preparation

Following the loading and unloading of the specimens, the DIC paint was removed using acetone and a cotton tipped wood probe and digital photographs were taken of the specimens. The specimens were then cut along horizontal and vertical initial cut lines shown in blue in Fig. 22. The section below the horizontal initial cut was not processed further. The right and left sections above the same line were pre-mounted in epoxy to prevent possible damage while further sectioning was performed. Next, three vertical sections labeled 'Surface', 'Quarter' and 'Center' were prepared for imaging. A secondary cut had to be made in order to be able to mount the 'Center' section. The horizontal section labeled 'Transverse' was also prepared for imaging. In a few of the specimens the secondary cut was avoided to image the transverse plane through half of the specimen thickness. Each section was mounted in epoxy and ground using 320 grit and then 600 grit SiC paper. The samples were then polished to a 1 μm finish on a Tegramin-30 automated polisher. Following that, the samples were placed on a 0.3 μm Al_2O_3 vibratory for 24 hours and then on a 0.04 μm SiO_2 vibratory for another 24 hours. Light optical images were taken of the areas of interest in all surfaces at 25X magnification. A few selected sites were also imaged at higher magnification. Some surfaces were later etched to reveal the grain structure. This was accomplished by using E407 #89 etchtant containing 10 mL HNO_3, 3 mL acetic acid, 15mL HCl and 2-5 drops of glycerol, immersing the parts for 15 seconds at a time until the grains were revealed, totaling approximately 45 seconds per sample.

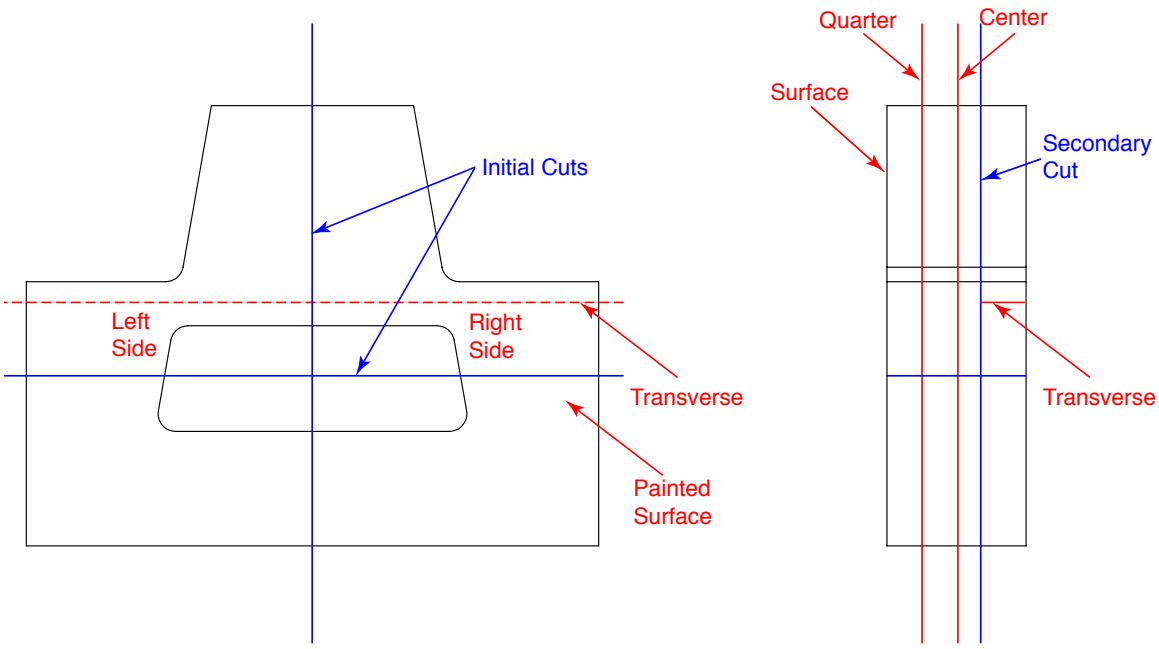

Figure 22: Schematic of specimens showing the locations of cuts and also the planes that were imaged for the metallography analysis.

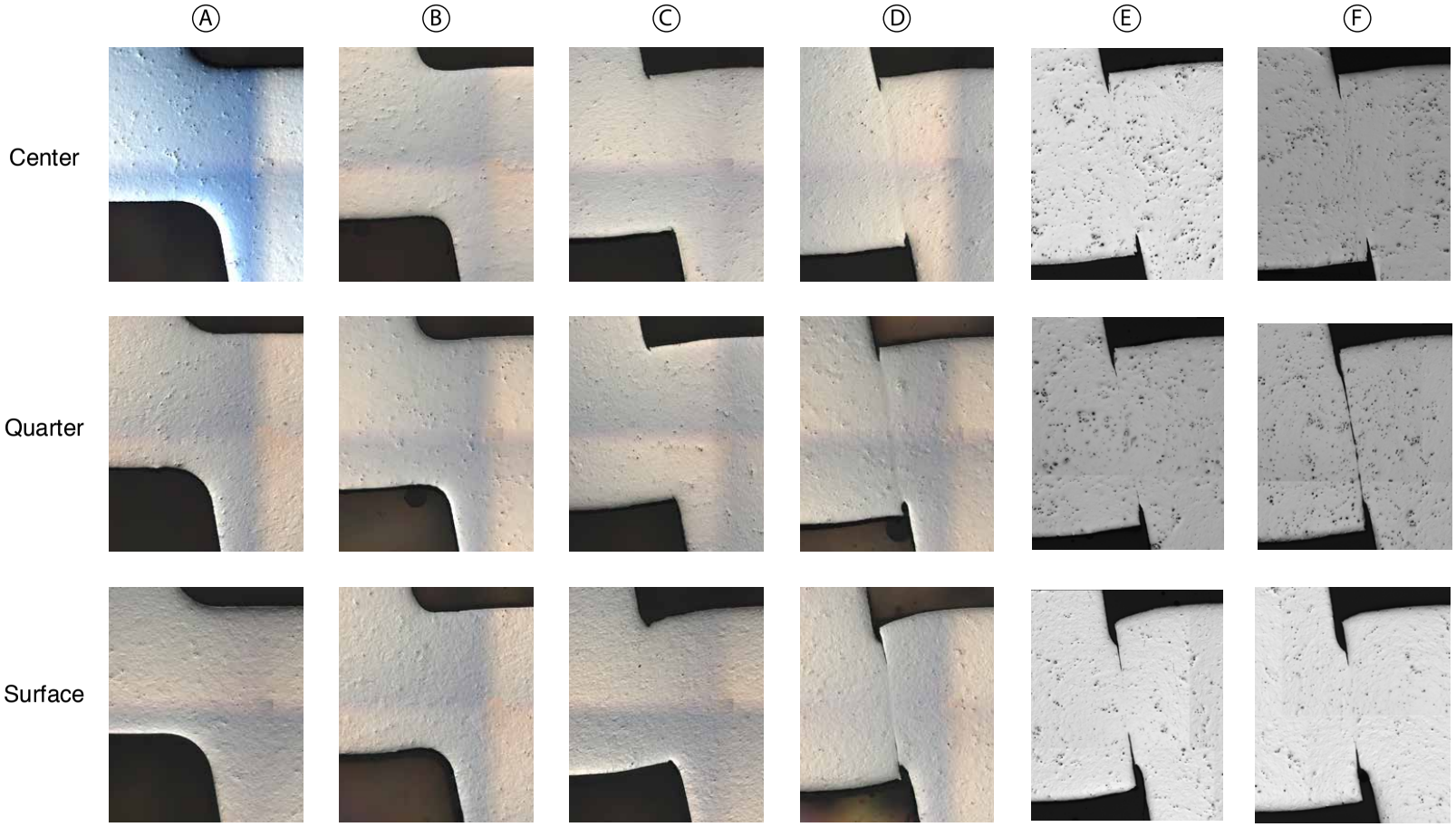

Figure 23: Montage showing micrographs of the right side taken for each steel specimen that was unloaded. The micrographs show the 'Center', 'Quarter' and 'Surface' planes defined in Fig. 22. The letters in the balloons correspond to the positions marked in Fig. 15.

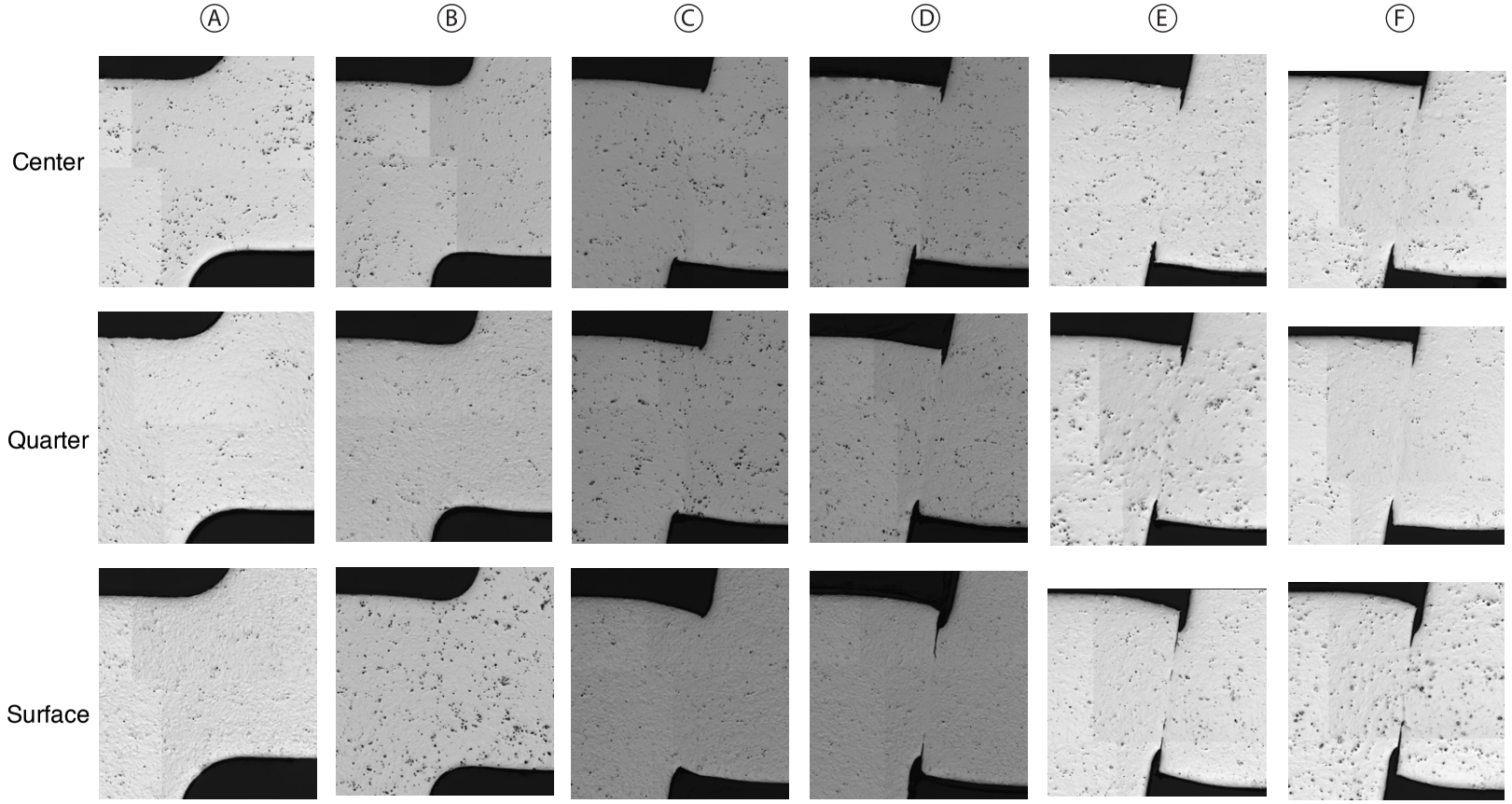

Figure 24: Montage showing micrographs of the left side taken for each steel specimen that was unloaded. The micrographs show the 'Center', 'Quarter' and 'Surface' planes defined in Fig. 22. The letters in the balloons correspond to the positions marked in Fig. 15.

Results

Figure 23 shows the images taken of the 'Surface', 'Quarter', and 'Center' surfaces on the right side of all specimens imaged. The letters in the balloons correspond to the points shown in Fig. 15, indicating progressively further loading from left to right. Figure 24 is similar, but for the left side of the specimen. The images under the labels Ⓐ and Ⓑ correspond to specimens unloaded while the $|P|$-$|\delta|$ response had positive slope. They show progressive deformation and sharpening of the radii in the specimens, but no cracks are apparent in any of the images. The first sign of damage occurred for the specimen unloaded from the vicinity of the maximum load, Ⓒ. By this point, the radii of the specimen had become almost sharp corners. What appear to be small 'indentations' are visible at those locations. This seems most noticeable in the 'Quarter' and 'Center' locations. Both the right and left sides of the specimen display similar features.

Specimens unloaded from the part of the $|P|$-$|\delta|$ curve with decreasing load exhibit progressive growth of the indentations on both the right and left sides. Note that the indentation depth is similar at all sections. 'Thin' cracks, however, can be seen emanating from the indentations by Ⓓ on the 'Surface' planes on both sides of the specimen. By this point, the load reduction is likely strongly influenced by crack growth eroding the load carrying capacity of the specimen.

Taking a closer look at what we have called indentations reveals what appear to be mode two cracks that generate longer new surfaces on one side of the crack than on the other. This can be most easily be seen in the 'Surface' images. At the top of the high deformation regions, the side of the indentation on the center section seems to be largely a part of the original surface of the the specimen while the side on the outer section appears to be a newly created surface. The opposite is true at the bottom of the same regions. The highly localized shear deformations in the high deformation zones likely provide the necessary kinematic accommodations to allow the relative sliding of the center section with respect to the outer sections of the specimen. Also note that the indentations look more blunt on the 'Surface' than on the 'Quarter' or 'Center' planes. In fact, even at Ⓒ, the radii at the center section on both sides of the specimen seem sharper at the center than at the other locations.

By Ⓔ the thin cracks also appeared in the 'Quarter' location of the right side, but not on the left side. This is the first clear sign of asymmetry in the specimens. Finally at Ⓕ, which corresponds to the specimen that was unloaded just prior to failure, the thin crack at the 'Quarter' location had penetrated almost the total length of the high deformation region on the right side, but the left side did not exhibit a thin crack at that location. There, the 'Surface' location shows a relative long sharp crack. Thin cracks were not seen in either of the 'Center' sections. The surface images at Ⓕ suggest that the apparent discontinuity of the marked line in Fig. 21 is a manifestation of a very high strain gradient.

A more quantitative assessment of the progression of deformation and damage was carried out by making measurements of the features shown in Fig. 25. These include a measure of deformation of the regions at the top and bottom of the areas of interest (ξ), the length of the

indentations (η) and the length of the thin cracks that emanated from the indentations (ζ). The subscripts u and l refer to the features in the upper and lower ends of the area of interest. Note that 'bridges' of continuous material sometimes interrupt the thin cracks, which could indicate that the cracks link up outside of the sectioning plane. The measurement ζ included only the thin crack segments adjacent to the indentations. Figure 26 shows the results of the measurements as functions of the platen displacement δ at the unloading point, normalized by the initial height of the region of interest (h =0.125 in). Note that the data show scatter and reversals in trends that one may expect to be monotonically increasing. This is partially due to the fact that the data came from six different specimens. Figures 26 (a) and (b) show that the deformation ξ increased with δ initially at all three sections, but the rate reduced considerably after the maximum load had been attained. Figures 26 (c) and (d) show that the length of the indentation η monotonically increased with δ, and that the growth was essentially the same at all locations monitored, although by the end the measurements at the 'Center' were a little smaller than elsewhere. Finally, Figs. 26 (e) and (f) show that the thin cracks did not appear until after the load maximum. They appeared first at the surface, and then later at some of the 'Quarter' sections. Their initial rate of growth seems to have been relatively fast. Therefore, one may conclude that after the maximum load, the continued growth of δ was significantly influenced by crack growth.

The remainder of this section will concentrate on details of the deformation, damage, and failure process that can be observed in images obtained at higher magnification. Referring back to Fig. 3, the CA prediction deviated from the experiments at a displacement that closely corresponded to the maximum displacement in S1, and the NM prediction deviated from the experiments at roughly half way between the maximum displacement in S1 and S2.

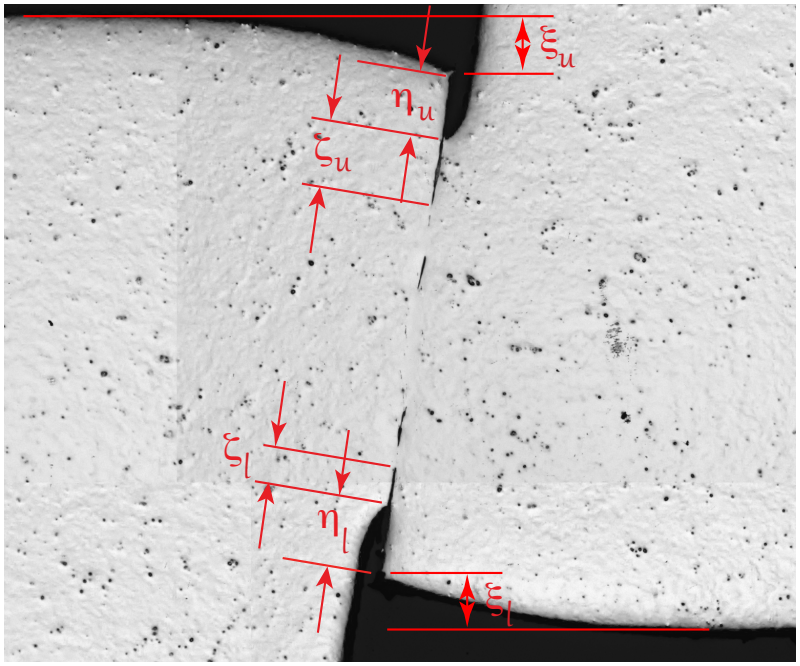

Figure 25: Definition of distances measured in the micrographs shown in Figs. 23 and 24.

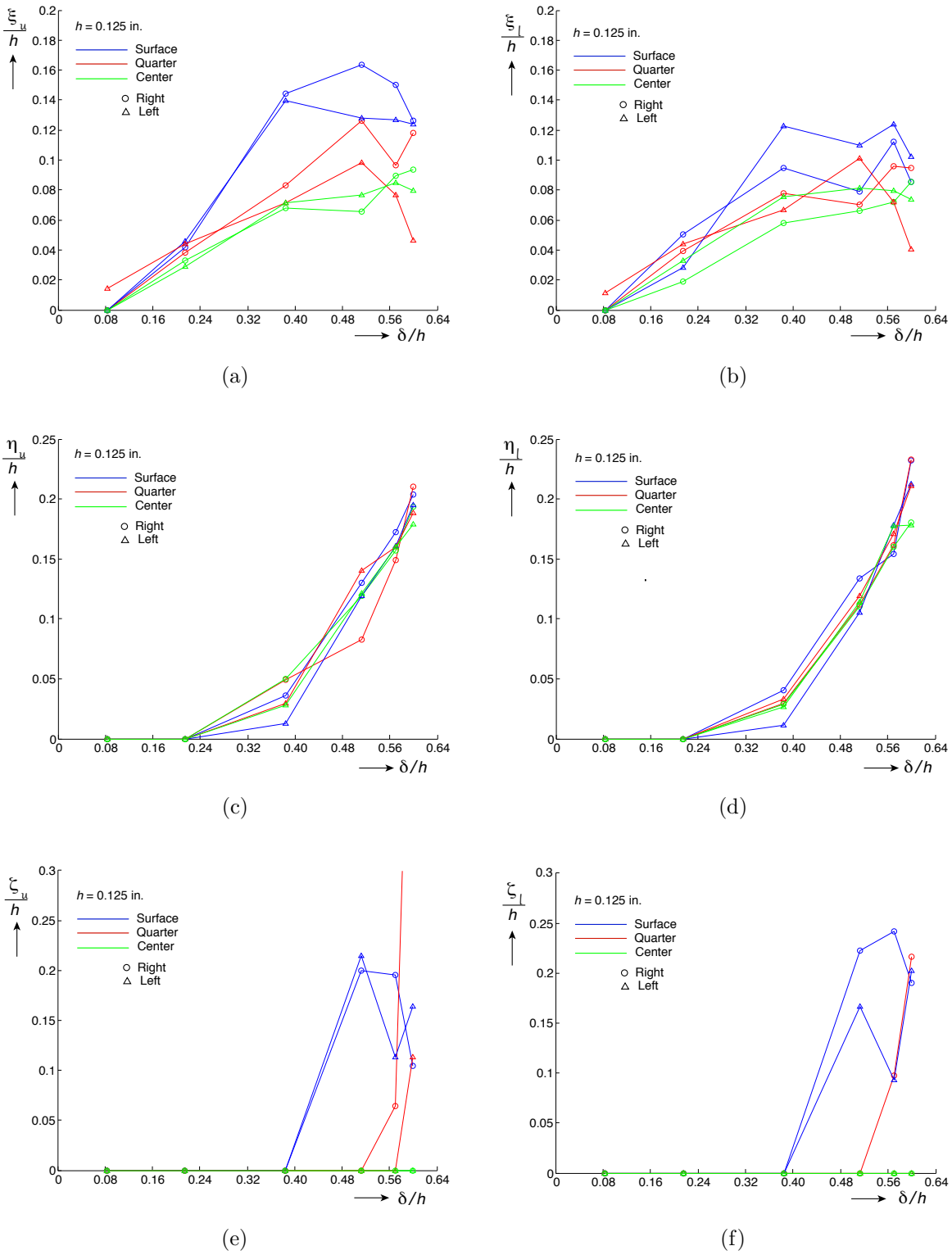

Figure 26: Distances measured from micrographs shown in Figs. 23 and 24 as functions of δ. (a) ξ_u, (b) ξ_l, (c) η_u, (d) η_l, (e) ζ_u and (f) ζ_l.

High magnification (200×) images of specimens S1 and S2 did not reveal signs of material damage in these specimens.

The first sign of damage appeared in specimen S3, which had the label Ⓒ in previous figures. This damage took the shape of small indentations at the edges of the high deformation region. In addition, specimen S3 also showed fracturing of carbide inclusions in the region of high deformation as shown in Fig. 27 (b). Away from this region, the inclusions were intact as shown in Fig. 27(a).

As deformation progressed and the applied load decreased, elongated cavities were observed. For example, Figure 28 shows a micrograph of the high deformation region at the center section of specimen S6. Although the indentations at the top and bottom of the image do not extend far into the sample, numerous elongated cavities or 'mini-cracks' are clearly visible. Images taken at even higher magnification on a different specimen, S5, show the character of these features in Figs. 29 (a) and (b). The elongated cavities seem to contain the debris of the broken carbide inclusions, thus indicating that they were indeed generated by the fracturing of the inclusions and became elongated due to the large deformation present.

The 'Center' and 'Quarter' sections of the right side of the most deformed specimens, S5 and S6, were etched in an attempt to reveal their deformed grain structure. The highly deformed grain structure proved difficult to interpret after etching as seen in Fig. 29. The lower magnification images in Fig. 30 show a more global picture of the microstructural deformation of specimen S5. The figures show a narrow dark region that is indicative of a region with large deformations. Interestingly, this region can also be seen to extend through the width of the specimen in the image labeled 'Transverse.' This image shows the surface of the similarly named plane described in Fig. 22 and is perpendicular to the plane of shear.

Finally, Fig. 31 shows the transverse, polished region of specimen S6. The width of this section is one half of the specimen thickness. It clearly shows the cracks that developed in the specimen at a depth around 1/8 of the thickness from the surface of the specimen. Not enough evidence exists to determine if these cracks actually represent sharp cracks that have bridged a significant length of the high deformation region or if they are just local features that appeared at the center of the specimen. They could be due to either, since both have been observed previously.

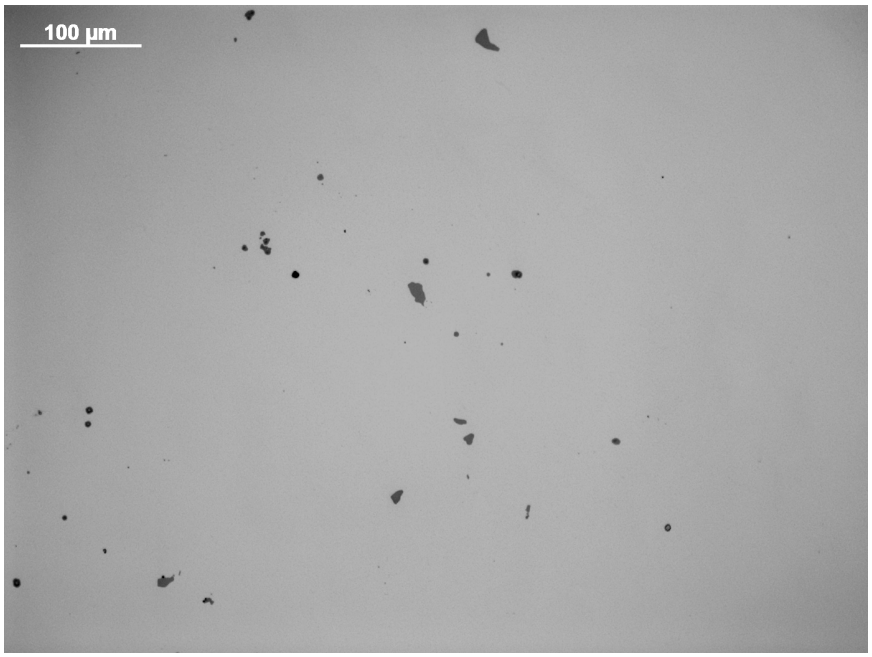

(a)

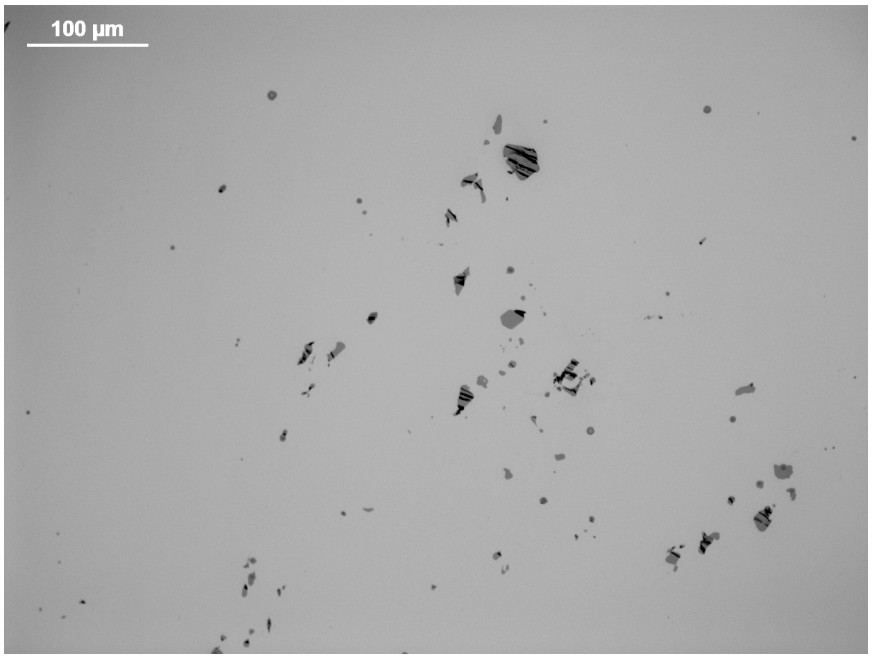

(b)

Figure 27: Micrographs from test S3 at a depth of one-half thickness. (a) Away from the zone of high deformation, showing intact carbide inclusions and (b) within the zone of high deformation, showing cracked carbide particles.

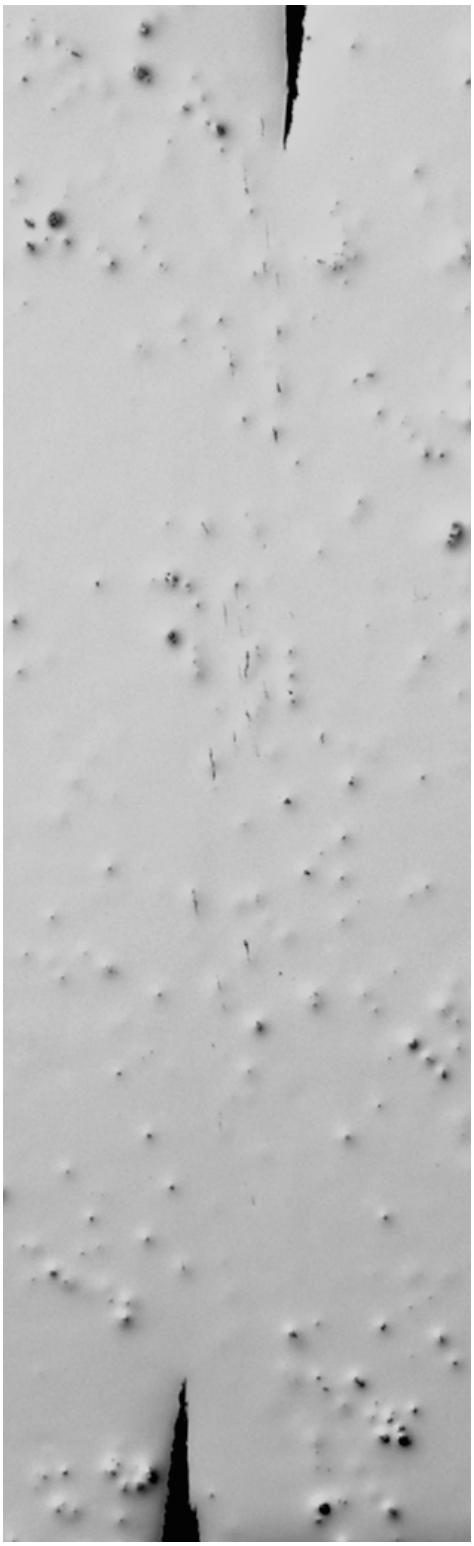

Figure 28: Section at a one-half thickness depth of specimens S6 prior to etching and showing the presence of small cracks near the center.

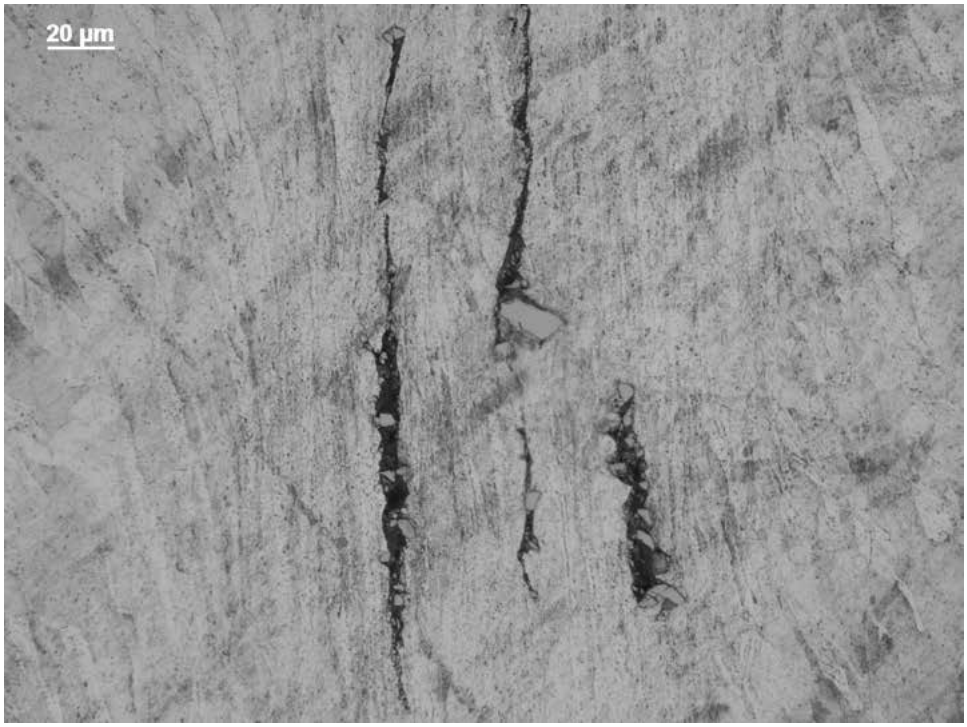

(a)

(b)

Figure 29: Detail from test S5 showing cracks initiated at carbide particles at a depth of one-quarter of the thickness. (a) Away from indentation features and (b) next to the indentation features.

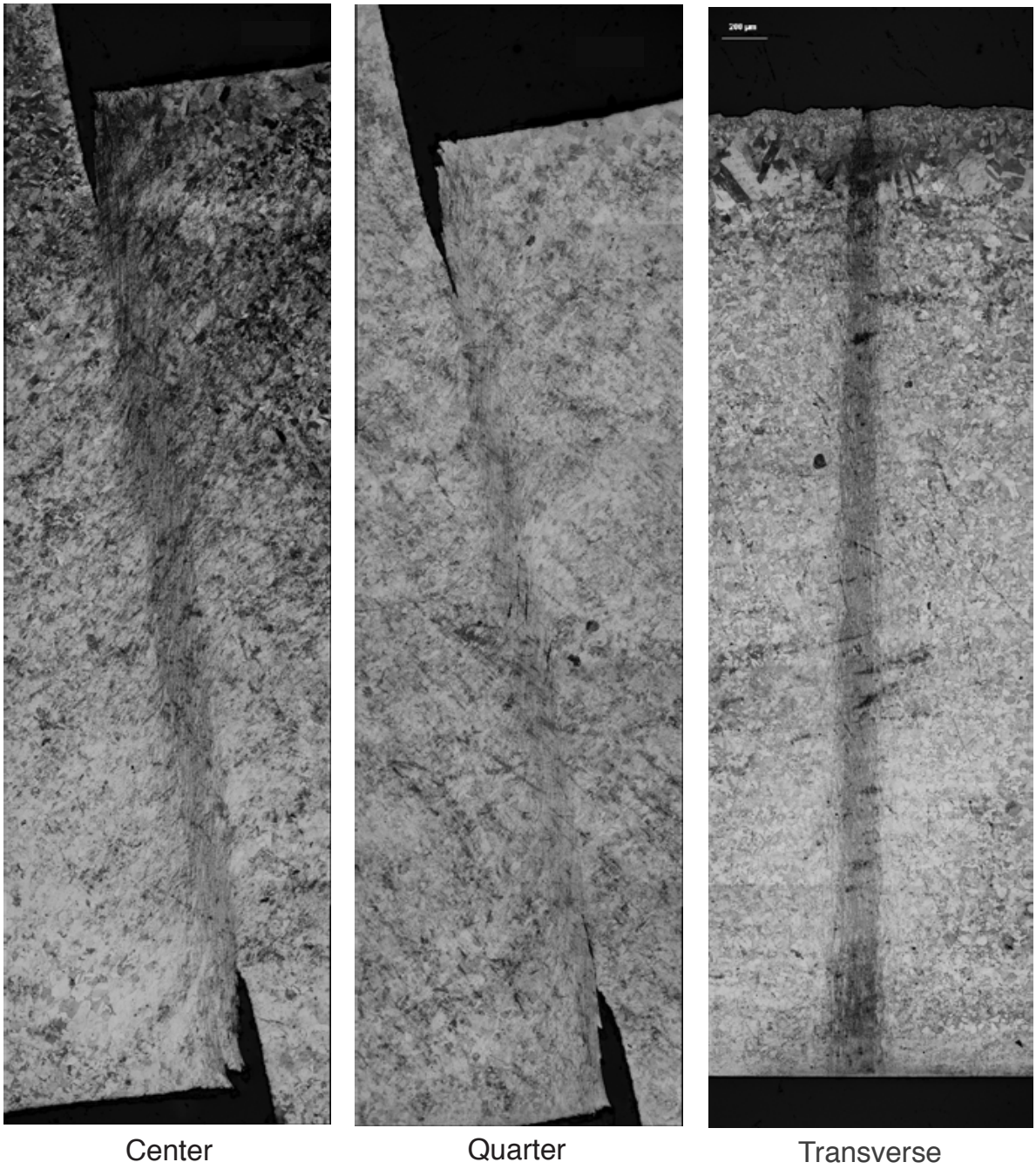

Figure 30: Magnified images of the failure zone for specimen S5 after etching. The figure also shows the image of the transverse cut.

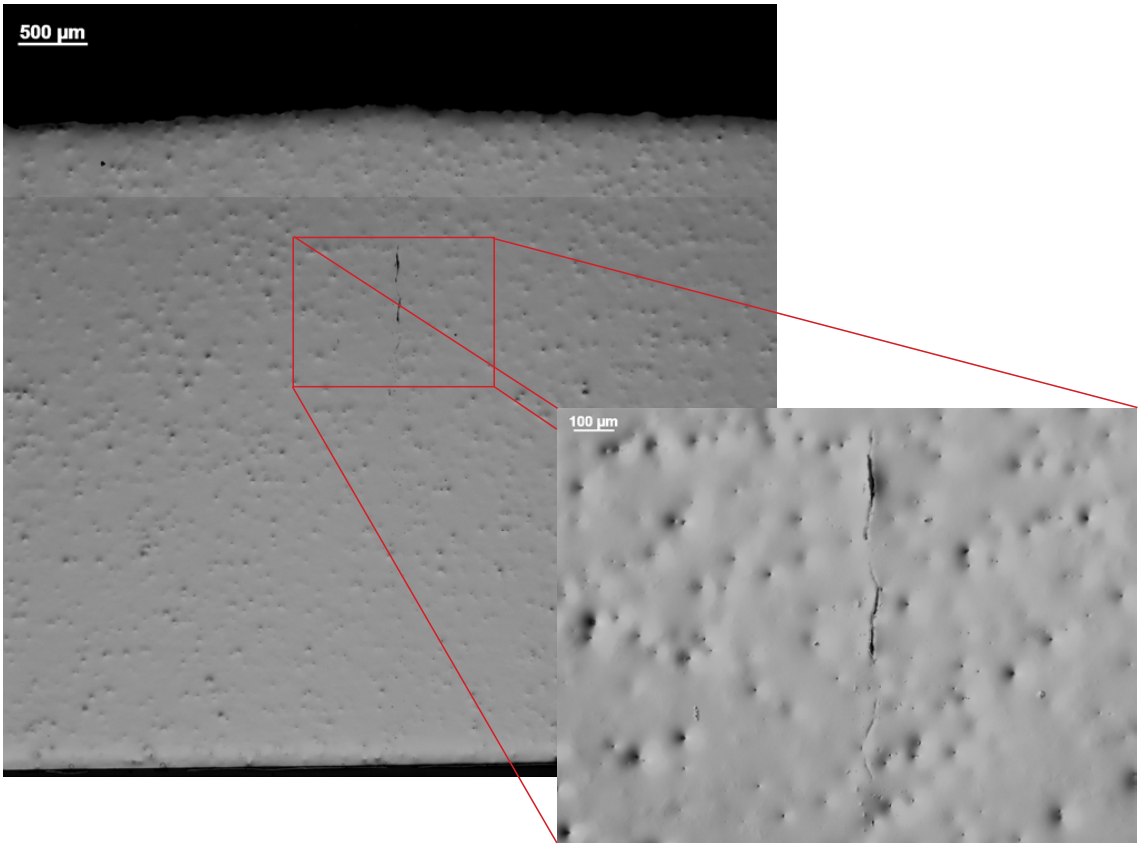

Figure 31: Detail of the transverse cut as shown in Fig. 22 showing that cracks have reached the mid-plane at locations between 1/8 and 1/4 of the thickness from the surface in specimen S6.

5 Results from Aluminum 7075-T651 Specimens

5.1 Fracture Surface Imaging

The aluminum specimens exhibited much simpler fracture surfaces, as in the example shown in Fig. 32, than corresponding images of the steel specimens in Fig. 12. Figure 32 shows a relatively smooth and uniform fracture surface with a few locations of some roughness. An interesting, and possibly significant, difference between the steel and aluminum specimens was that while the steel specimens broke apart at failure, thus exposing the fracture surfaces an both left and right sides, the aluminum specimens remained in one piece after failure. In other words, at failure the load dropped to zero, and cracks could clearly be seen on the surface, but the center part did not break away from the rest of the specimen. After sectioning the lower part of the specimen, it was possible to expose the fracture surfaces, but a little finger pressure was required to separate the center section from the outside section. Visual comparison between the fracture surfaces on the outside left and right sections showed few differences, unlike in the steel specimens.

Figure 32: Fracture surface from aluminum specimen A7.

Figure 33 shows a series of SEM images of the fracture surface in Fig. 32 taken at progressively higher magnification. The top image shows an area where the surface is relatively smooth, but it reveals a number of cavities that are sparsely distributed and possibly formed by inclusions that were originally present in the material. The smooth areas have some structure and display what appear to be vertical scouring marks aligned with the direction of shearing as seen in the middle picture. These may indicate rubbing between the mating surfaces at failure. This picture also shows some of the cavities in more detail as well as a 'fuzzy' region on the right side of the rectangle. This fuzzy region is shown at higher magnification in the lower image, revealing a field of very small dimples that seem to show a preferential orientation, also aligned with the direction of shear.

Not enough information is available in the SEM images to make statements as to how failure initiated and progressed in these specimens. It is also possible, and perhaps likely, that rubbing between the surfaces at failure erased the initial relief of the fracture surfaces.

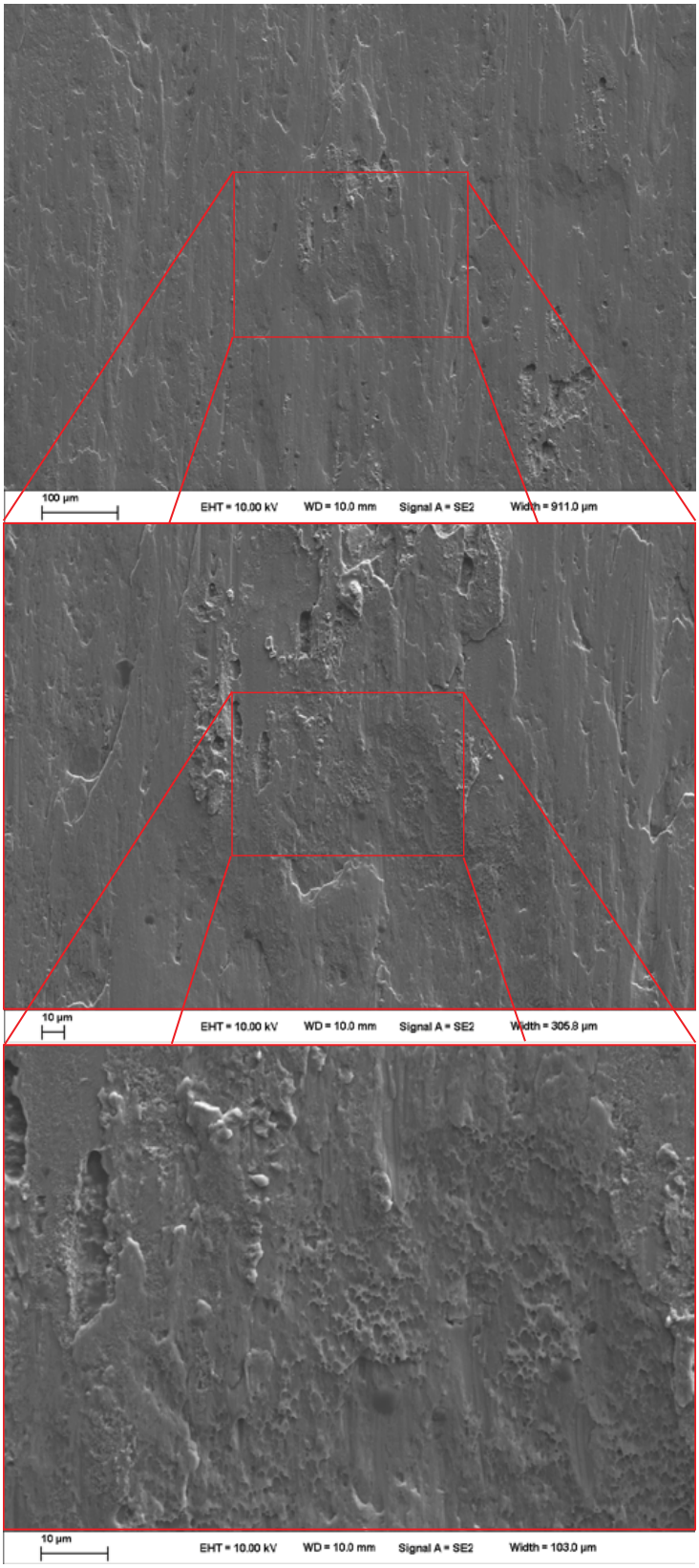

Figure 33: Higher magnification images of the fracture surface of aluminum specimen A7.

5.2 Material Uniaxial Stress-Strain Response

Figure 34 shows the results of three uniaxial tension tests conducted on specimens cut in the plane of the plate and at different orientations with respect to the rolling direction. The specimen direction is indicated by the angle that the axis of the specimen made with the rolling direction. Referring back to Fig. 1 the rolling direction coincided with the Y direction. The specimens had the same design as in Fig. B.2 in Appendix B. The nominal strain rate in these tests was 0.16×10^{-3} 1/s.

Clearly, this material also shows signs of anisotropy, with the 45° specimen exhibiting lower flow stress and higher elongation to failure. These complexities in the behavior of the material were not accounted for in the puncture simulations in [6]. Results of other tests used to characterize this alloy are presented in that reference. The observed overestimation of the load in Fig. 6 is most likely due to the observed lower yield stress of the 45° specimen. Little can be said about failure since our understanding of that field is still incomplete.

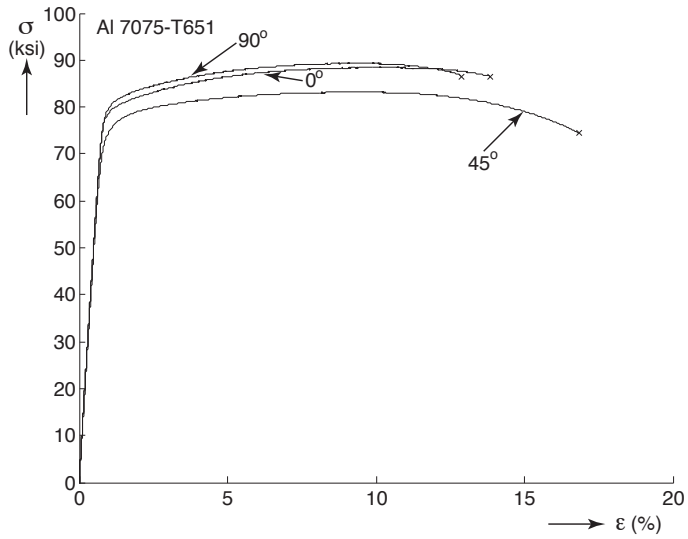

Figure 34: Uniaxial engineering stress-strain curves for Al 7075-T651 coupons cut along three in-plane directions (labeled in reference to the rolling direction). The coupons came from the same plate as the compression specimens.

5.3 Shear Dominated Compression Specimen Investigation

A total of seven tests were conducted for the aluminum specimens. The load-deflection curves are presented in Fig. 35. The procedure in four cases A1, A2, A3 and A4 was to load to a pre-determined value of platen displacement and then unload so the specimens would be available for sectioning. Two of the specimens, A6 and A7, were loaded to failure at rates of 0.001 and 0.0001 in/s respectively. Note that while specimen A6 failed while the load was increasing, specimen A7 developed a force maximum followed by a brief period where the

load decreased. Specimen A5 was unloaded at a point that was deemed to be close to failure, just past the maximum load.

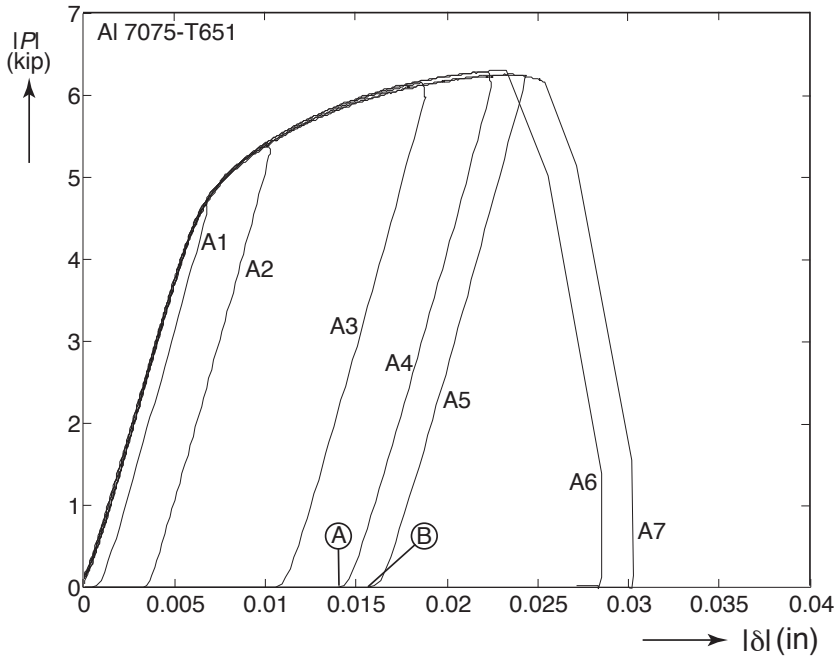

Figure 35: Load vs. platen relative displacement (average of four LVDT signals) for all tests conducted on Aluminum 7075-T651. The extent of compression is clearly seen for all specimens tested.

The platen displacement measurement δ is compared against the relative displacement of the fiducials δ_e for test A6 in Fig. 36. The difference is similar to that seen in Fig. 17 for the steel specimen. Similar to the steel specimens, the platen displacement measurement is sufficient for the purposes of this report, but future modeling efforts may wish to also compare against the fiducial displacement.

DIC Analysis Results

Figure 37(a) shows the force-displacement curve for experiment A6 with four points corresponding to the DIC strain measurements in Fig. 37(b). As in the case of the steel specimens, the strain concentrated in a narrow band as shown. All three surface strain components developed gradually but with accentuating gradients until point ③ just prior to failure of the specimen. At this point the maximum as-measured shear strain component was in the vicinity of 20% while the maximum normal strain component values were approximately one-half of the shear component. Failure of the specimen came with no warning just after point ③.

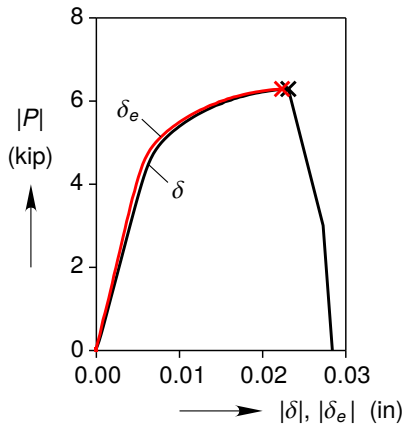

Figure 36: A comparison of the platen displacement δ against the relative displacement of the fiducials δ_e in test A6.

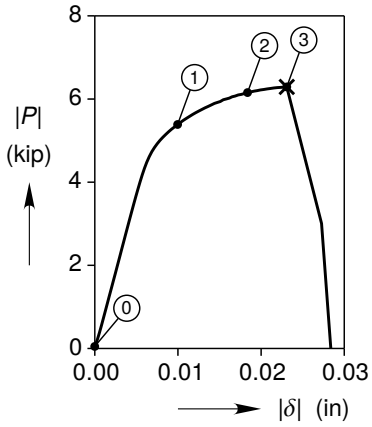

(a)

Figure 37: DIC results for experiment A6. (a) Load-deflection response. The numbers in the balloons correspond to the images shown in (b).

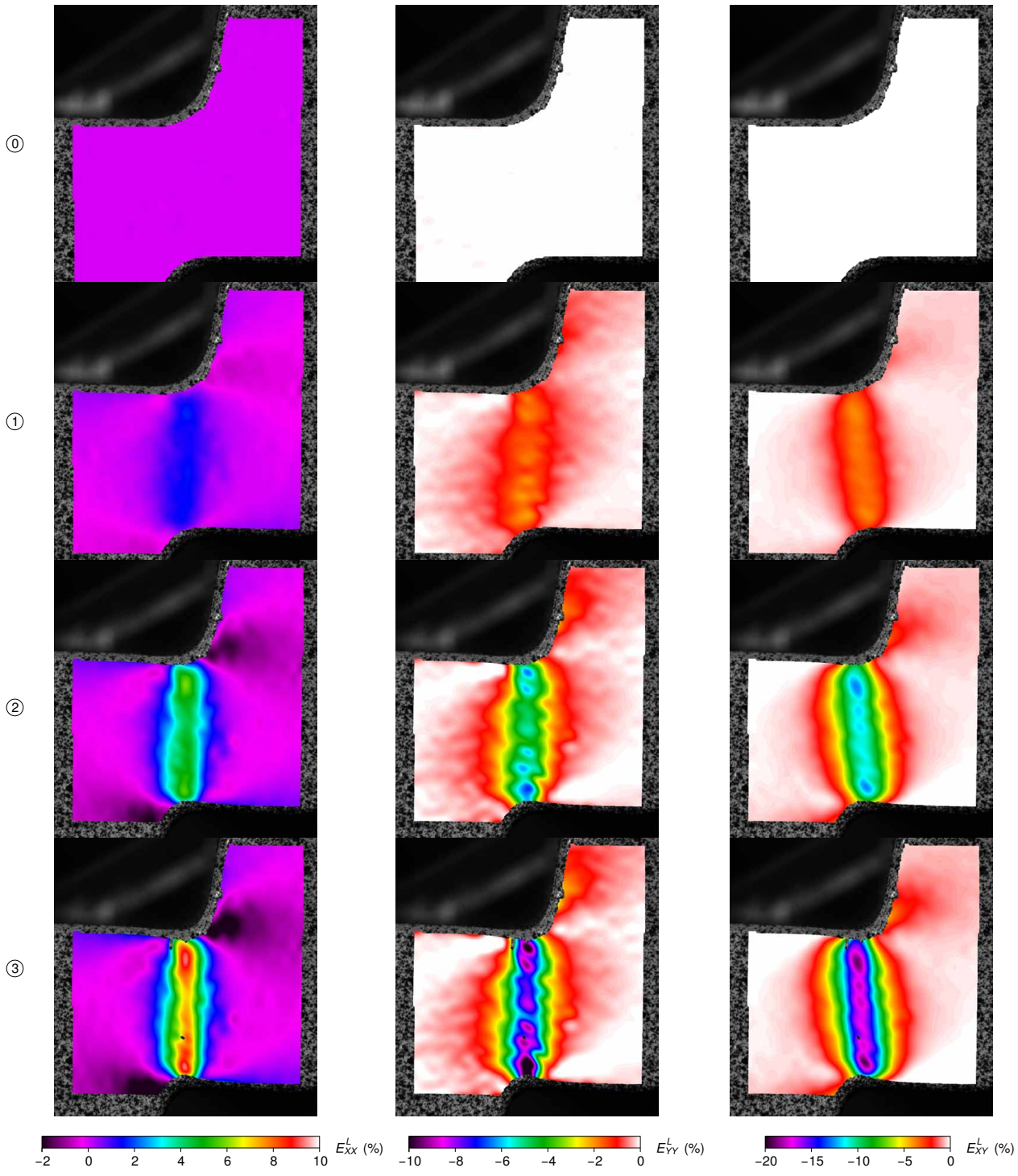

(b)

Figure 37: **(continued)** (b) Surface logarithmic strain components. X and Y represent the horizontal and vertical directions, respectively at the points marked in (a).

Metallography Analysis

The analysis was conducted in the same manner as for the steel specimens, but only the specimens with the largest displacements before unloading were examined. Figure 38 shows micrographs of the polished right front side of the specimen for specimens A4 and A5, A and B respectively in Fig. 35. The unloading point for specimen A4 was just prior to the displacement where specimen A6 failed while the unloading point of specimen A5 was just after it achieved its load maximum. Recall that the loading rates were different, 0.001 in/s for A4 and 0.0001 in/s for A5. The three sections shown for each case are: at the center of the specimen, at a depth of one-quarter of the thickness and at the surface. No evidence of cracks can be seen in any of the micrographs. This indicates that failure of the specimens occurred in a rather sudden manner, with an essentially immediate transition between first failure in the specimen and catastrophic failure. Figure 39 shows the same surfaces shown in Fig. 38 after etching to reveal the grain structure. The images do not reveal anything suggesting the impending failure of the specimens. This is the reason why specimens unloaded from lower deflections were not sectioned and imaged.

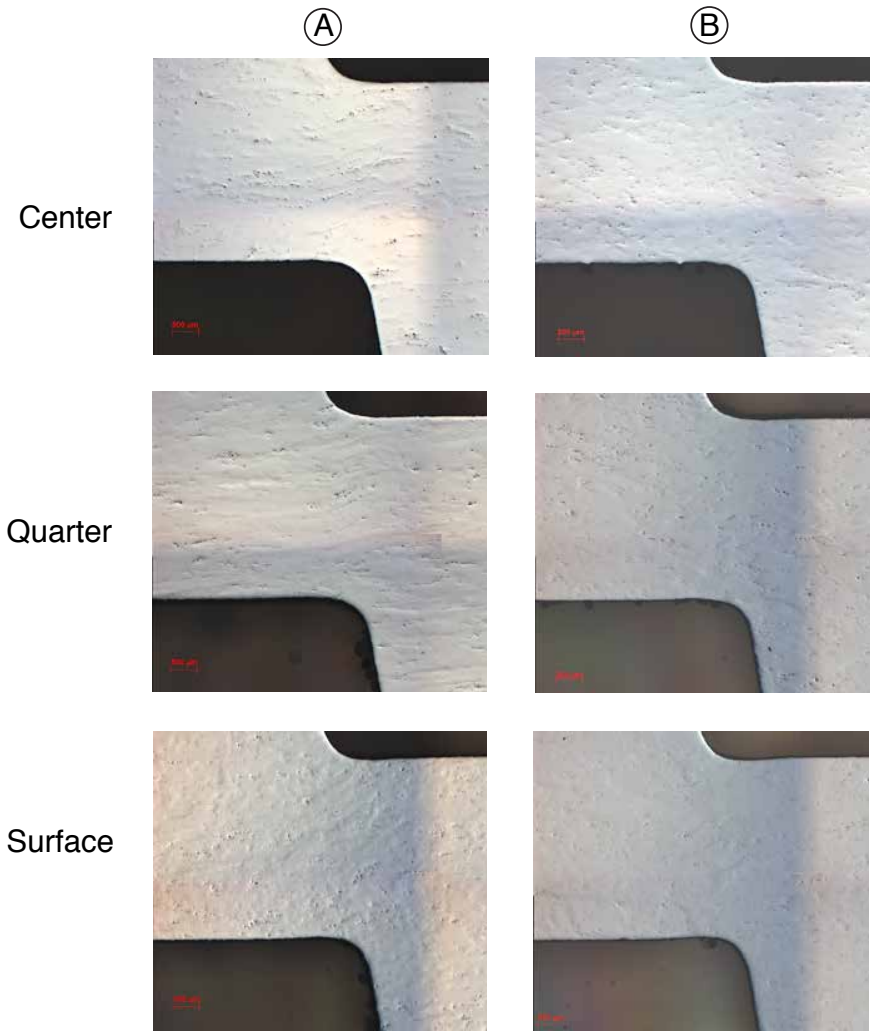

Figure 38: Montage showing micrographs taken for the two most deformed aluminum specimens that were unloaded. The micrographs show images of the three planes defined in Fig. 22. The letters in the balloons correspond to the points marked in Fig. 35 (b).

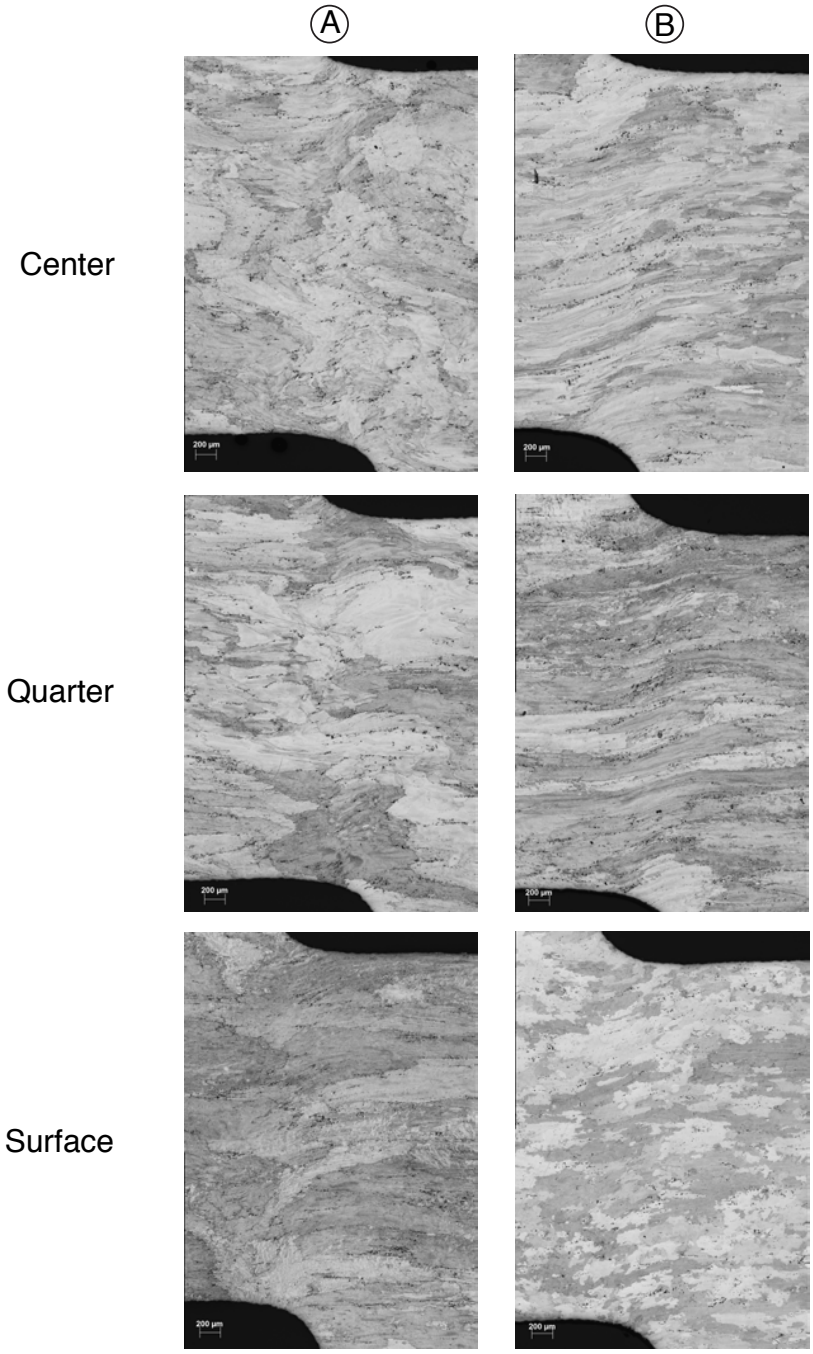

Figure 39: Micrographs of the two most deformed aluminum specimens after etching to reveal the grains. The images correspond to the three planes defined in Fig. 22.

6 Conclusions

This report addressed an experimental study of the failure of the 2013 Sandia Fracture Challenge shear-dominated compression specimens. Poor comparison between predicted and experimental results motivated the current study to experimentally address the deformation and failure of the specimens. While the specimens used in the 2013 fracture challenge competition were made from A286 steel, a second series of tests was conducted on Al 7075-T651 specimens to investigate the behavior of this alloy under high shear conditions.

A286 Steel Specimens

Uniaxial tension tests on the A286 steel specimens indicated that yield anisotropy was present in the material. While the stress-strain curves of specimens aligned with the length and width of the plate used to manufacture the specimens were similar, the stress-strain curves of specimens cut at 45° to these directions showed significantly lower flow stress. The numerical predictions that motivated this work did not include yield anisotropy, and this could be one of the factors affecting the quality of the simulations.

Testing of the shear-dominated compression specimens involved eight specimens. Two of them were compressed to failure. The load-deflection response was characterized by a load maximum followed by a slow load decrease that continued until failure occurred. DIC-based estimation of the logarithmic strain components on the surface of the high deformation region showed that all components had magnitudes in the order of 50% when the load maximum occurred. Strain measurements became quite unreliable past this point because of the very high deformation gradients that developed.

The reminder of the specimens were compressed to a pre-determined displacement, smaller than the displacement at failure, and were then unloaded. These specimens were then sectioned in order to look for evidence of damage via microscopy studies. No evidence of cracks or material damage was observed for the two specimens unloaded prior to the maximum load. The specimen unloaded from the vicinity of the maximum load showed small indentations at either end of the high deformation region as well as cracking of carbide inclusions in the same region. The indentations were progressively deeper for specimens unloaded after the maximum load and narrow cracks appeared on the surface of the specimens and at a depth of 1/4 of the specimen thickness as the catastrophic failure point was approached.

Going back to the predictions of the load-deflection response by the NM team in Fig. 3, current observations indicate that the deviation from the experiment was not due to material damage. Instead, it is more likely that it was influenced by material anisotropy and also by perhaps having used too coarse a mesh that did not allow sufficient sharpening of the radii of the specimens within the high deformation region. Future numerical simulations will address both of these issues in an effort to improve the results, at least up until the load maximum. Prediction of the part of the response with decreasing load will be even more challenging as it involves the initiation and propagation of material failure.

Al 7075-T651 Specimens

The behavior of the aluminum specimens was considerably different from that of the steel ones. From the point of view of the load-deflection response, the principal difference concerned the much lower platen displacements of the aluminum specimens when failure occurred, only about 30% of those of the steel specimens. In addition, failure occurred either with an increasing load, or almost immediately after a load maximum was identified. Given the relatively small platen displacements, the strain components on the surface of the specimens were in the order of 20% right before failure. It is also worth noting that the metallographic analysis did not reveal any visible damage in the specimens just prior to failure.

The results obtained in this work provide experimental evidence of the behavior and failure of the two alloys considered. In one case, the response and failure exhibited significantly ductile characteristics while the other exhibited significantly less ductility. The deformation and failure of the specimens have been documented in as much detail as could be reasonably expected for a project of this scope. The data provided will be used in the future to evaluate the quality of numerical predictions and the capabilities of constitutive and failure models used to represent material behavior.

References

[1] Boyce, B.L., Kramer, S.B.L., Fang, H.E., Cordova, T.E., Neilsen, M.K., Dion, K., Kaczamrowski, A.K., Karasz, E., Xue, L., Gross, A.J., Ghahremaninezhad, A., Ravi-Chandar, K., Lin, S.-P., Chi, S.-W., Chen, J.S., Yreux, E., Ruter, M., Qian, D., Zhou, Z., Bhamare, S., O'Connor, D.T., Tang, S., Elkhodary, K.I., Zhao, J., Hochhalter, J.D., Cerrone, A.R., Ingraffea, A.R., Wawrzynek, P.A., Carter, B.J., Emery, J.M., Veilleux, M.G., Yang, P., Gan, Y., Zhang, X., Chen, Z., Madenci, E., Kilic, B., Zhang, T., Fang, E., Liu, P., Lua, J., Nahshon, K., Miraglia, M., Cruce, J., DeFrese, R., Moyer, E.T., Brinckmann, S., Quinkert, L., Pack, K, Luo, M. and Wierzhicki, T. 2014. The Sandia Fracture Challenge: blind round robin predictions of ductile tearing, *International Journal of Fracture*, **186**, pp. 5–68, 2014.

[2] High Temp Metals, A-286 technical data. 2015. www.hightempmetals.com/techdata/hitempA286data.php.

[3] Wellman, G.W. 2012. A simple approach to modeling ductile failure, Technical Report SAND12-1343, Sandia National Laboratories, Albuquerque, NM

[4] Ghahremaninezhad, A. and Ravi-Chandar, K. 2011. Ductile failure in polycrystalline OFHC copper. *International Journal of Solids and Structures*, **48**, pp. 3299-3311.

[5] Corona,E., Witkowski, W.R., Breivik, N.L., Hu, K.T., Gorman, J.S., Spletzer, M.A. and Cordova, T.E. 2012. ASC V&V L2 Milestone No. 4485: Puncture failure predictions, Technical Report SAND2012-7604, Sandia National Laboratories, Albuquerque, NM

[6] Corona, E. and Orient, G.E. 2014. An evaluation of the Johnson-Cook model to simulate puncture of 7075 aluminum plates, Technical Report SAND2014-1550, Sandia National Laboratories, Albuquerque, NM.

[7] Correlated Solutions. 2012. Vic-3D Manual. Correlated Solutions, Inc., Columbia, SC.

[8] Sutton, M.A., Orteu, J.J., Schreier, H.W. 2009. Image Correlation for Shape, Motion, and Deformation Measurements: Basic Concepts, Theory, and Applications. Springer, New York.

[9] Correlated Solutions. 2009. Vic-2D Manual. Correlated Solutions, Inc., Columbia, SC.

[10] Kerlins, V. and Phillips, A. 1987. Modes of Fracture, Metals Handbook, Volume 12: Factography, Ninth Edition, ASM International.

A Heat Treatment and Microstructure of Steel A286 Specimens

Figure A.1 shows the heat treatment record of the plate from which all steel specimens were manufactured while Fig. A.2 (a) shows the microstructure of the steel A286 material. It shows relatively equi-axed grains, but with some regions where the grains have larger sizes than in general. The material also included some fairly large second phase carbide particles pointed out in Fig. A.2 (b).

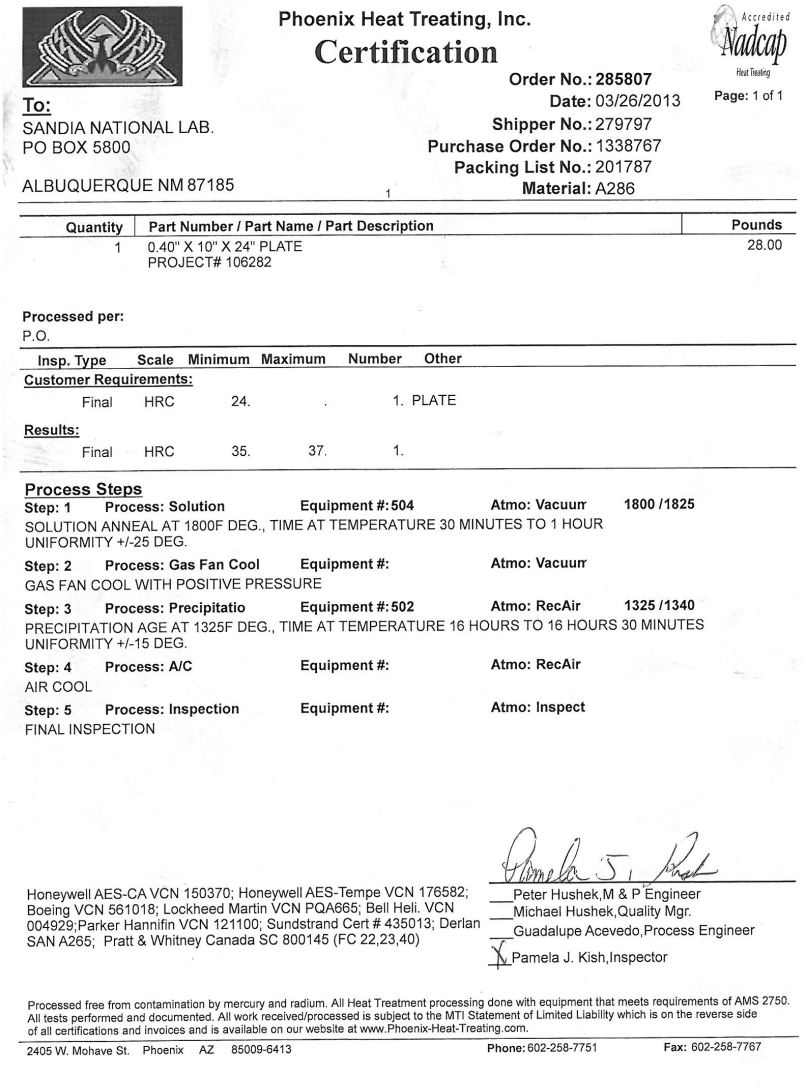

Phoenix Heat Treating, Inc.

Certification

Accredited Nadcap Heat Treating

Page: 1 of 1

To:
SANDIA NATIONAL LAB.
PO BOX 5800

ALBUQUERQUE NM 87185

Order No.: 285807
Date: 03/26/2013
Shipper No.: 279797
Purchase Order No.: 1338767
Packing List No.: 201787
Material: A286

Quantity	Part Number / Part Name / Part Description	Pounds
1	0.40" X 10" X 24" PLATE PROJECT# 106282	28.00

Processed per:
P.O.

Insp. Type	Scale	Minimum	Maximum	Number	Other
Customer Requirements:					
Final	HRC	24.	.	1.	PLATE
Results:					
Final	HRC	35.	37.	1.	

Process Steps

Step: 1 **Process: Solution** **Equipment #: 504** **Atmo: Vacuum** **1800 /1825**
SOLUTION ANNEAL AT 1800F DEG., TIME AT TEMPERATURE 30 MINUTES TO 1 HOUR
UNIFORMITY +/-25 DEG.

Step: 2 **Process: Gas Fan Cool** **Equipment #:** **Atmo: Vacuum**
GAS FAN COOL WITH POSITIVE PRESSURE

Step: 3 **Process: Precipitatio** **Equipment #: 502** **Atmo: RecAir** **1325 /1340**
PRECIPITATION AGE AT 1325F DEG., TIME AT TEMPERATURE 16 HOURS TO 16 HOURS 30 MINUTES
UNIFORMITY +/-15 DEG.

Step: 4 **Process: A/C** **Equipment #:** **Atmo: RecAir**
AIR COOL

Step: 5 **Process: Inspection** **Equipment #:** **Atmo: Inspect**
FINAL INSPECTION

Honeywell AES-CA VCN 150370; Honeywell AES-Tempe VCN 176582; Boeing VCN 561018; Lockheed Martin VCN PQA665; Bell Heli. VCN 004929;Parker Hannifin VCN 121100; Sundstrand Cert # 435013; Derlan SAN A265; Pratt & Whitney Canada SC 800145 (FC 22,23,40)

Peter Hushek,M & P Engineer
Michael Hushek,Quality Mgr.
Guadalupe Acevedo,Process Engineer
X Pamela J. Kish,Inspector

Processed free from contamination by mercury and radium. All Heat Treatment processing done with equipment that meets requirements of AMS 2750. All tests performed and documented. All work received/processed is subject to the MTI Statement of Limited Liability which is on the reverse side of all certifications and invoices and is available on our website at www.Phoenix-Heat-Treating.com.

2405 W. Mohave St. Phoenix AZ 85009-6413 **Phone:** 602-258-7751 **Fax:** 602-258-7767

Figure A.1: Heat treatment record of the plate from which all steel specimens were machined.

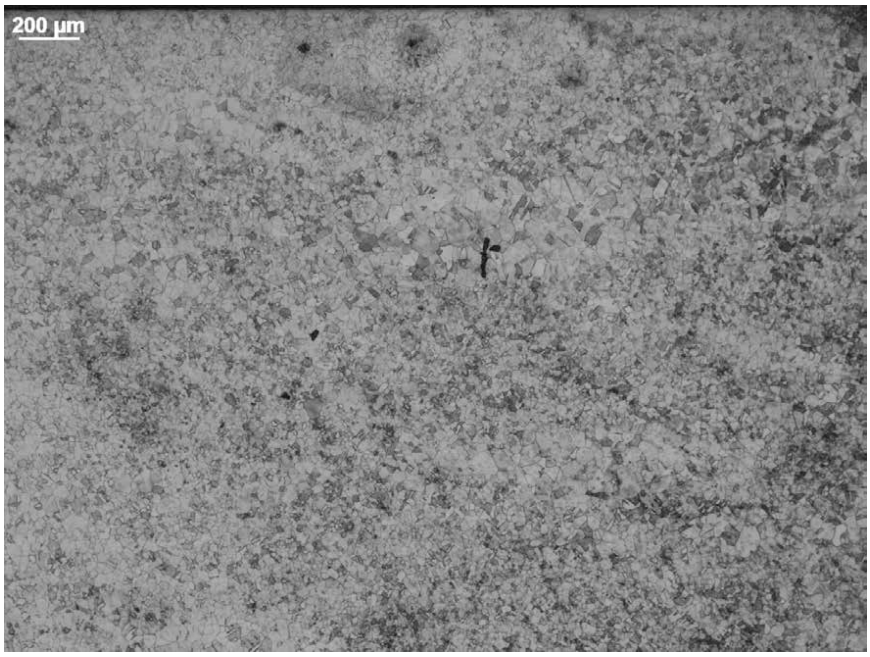

(a)

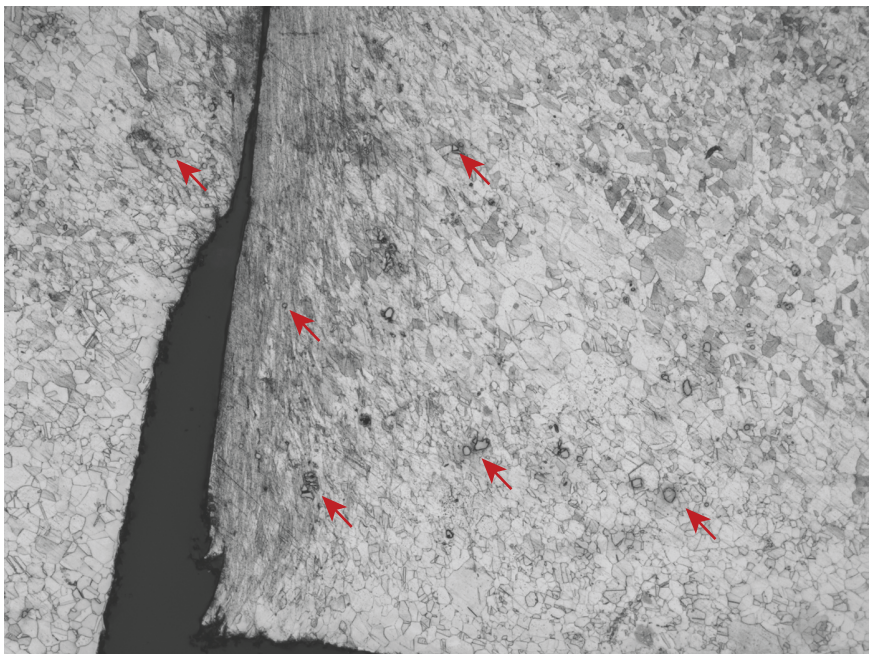

(b)

Figure A.2: Material microstructure in the steel A286 specimens. (a) Image showing mostly equiaxed austenite grains with some duplexed grain structure and (b) image highlighting some of the fairly large second phase carbide particles.

B Dimensions of Uniaxial Tension Test Specimens

Figures B.1 and B.2 show the prints based on which the uniaxial tension tests specimens for steel A286 and Al 7075-T65, respectively, were manufactured. The dimensions are given in inches.

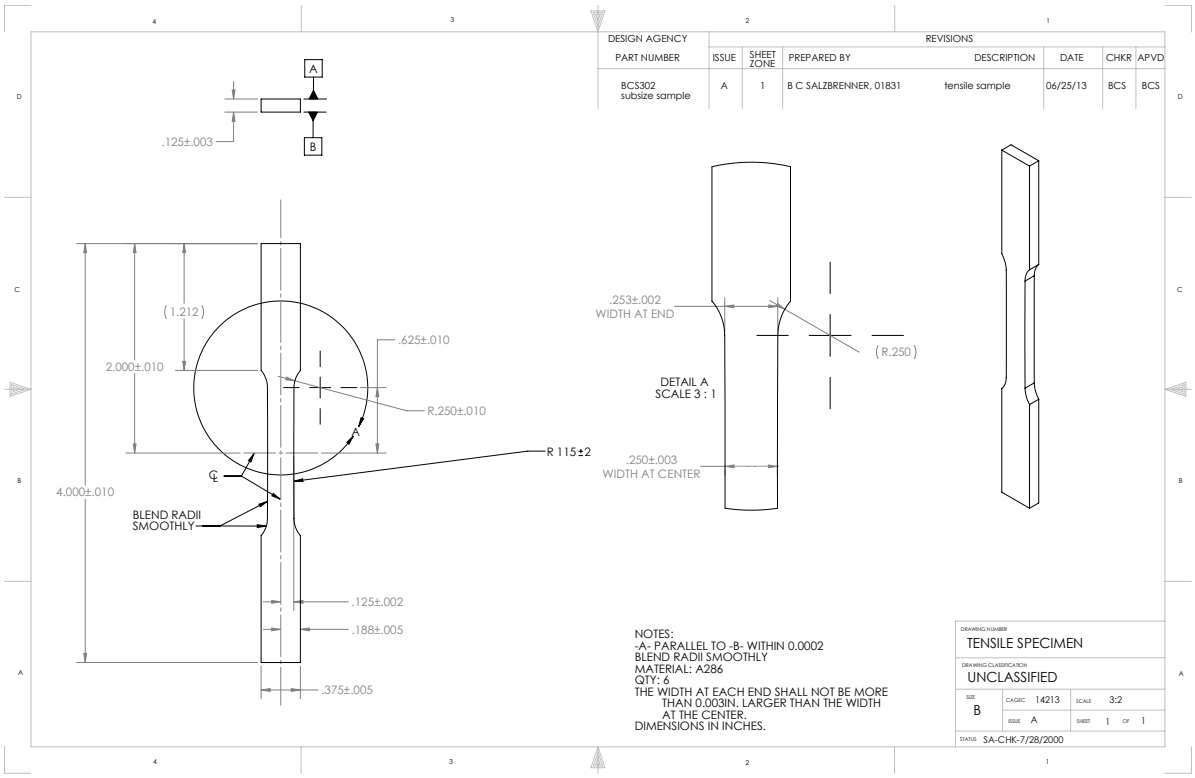

Figure B.1: Print for the flat specimens used in uniaxial tension testing of steel A286.

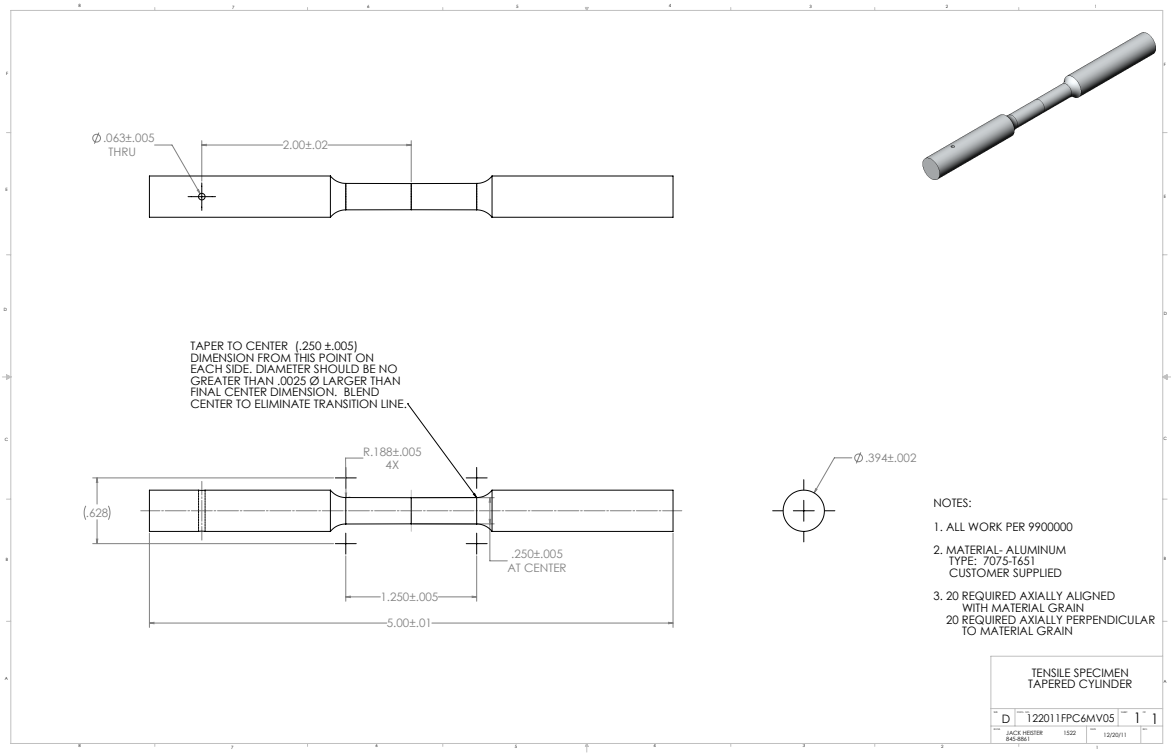

Figure B.2: Print for the cylindrical specimens used in uniaxial tension testing of Al 7075-T651.

C Experiment Numbers

Table C.1 presents the correspondence between the experiment labels used in this report and the original numbers that are also used to archive the results in the Structural Mechanics Laboratory.

Table C.1: Correspondence between experiment labels in this report and the Structural Mechanics Laboratory archive.

Report	SML Archive
S1	B9
S2	B4
S3	B5
S4	B6
S5	B8
S6	B1
S7	B3
S8	B10
A1	A7
A2	A10
A3	A2
A4	A8
A5	A6
A6	A5
A7	A1

DISTRIBUTION:

1 MS 0346 M. Neilsen, 1526
1 MS 0346 J. Emery, 1526
1 MS 0557 J. Gorman, 01558
1 MS 0557 S. Kramer, 01558
1 MS 0744 J. Bignell, 6233
1 MS 0744 C. Jones, 6233
1 MS 0747 R. Dngreville, 6233
1 MS 0748 S. Sanborn, 6233
1 MS 0815 J. Johannes, 1500
1 MS 0828 G. Orient, 1544
1 MS 0840 J. Redmond, 1550
1 MS 0840 D. Aragon, 1554
1 MS 0840 J. Arguello, 1554
1 MS 0840 J. Bean, 1554
1 MS 0840 J. Bishop, 1554
1 MS 0840 N. Breivik, 1554
1 MS 0840 E. Corona, 1554
1 MS 0840 J. Cox, 1554
1 MS 0840 J. Dempsey, 1554
1 MS 0840 H. Fang, 1554
1 MS 0840 S. Grange, 1554
1 MS 0840 K. Gwinn, 1554
1 MS 0840 C. Hammetter, 1554
1 MS 0840 T. Hinnerichs, 1554
1 MS 0840 C. Lo, 1554
1 MS 0840 J. Bishop, 1554
1 MS 0840 K. Long, 1554
1 MS 0840 P. Newell, 1554
1 MS 0840 B. Reedlunn, 1554
1 MS 0840 W. Scherzinger, 1554
1 MS 0840 J. Pott, 1555
1 MS 0886 L. Deibler, 1819
1 MS 0886 S. Williams, 1819
1 MS 0889 B. Boyce, 1831
1 MS 0889 J. Carroll, 1851
1 MS 1031 M. Ingraham, 6914
1 MS 9035 M. Maguire, 1831

1	MS 9042	A. Brown, 8259
1	MS 9042	M. Chiesa, 8259
1	MS 9042	K. Dion, 8259
1	MS 9042	K. Karlson, 8259
1	MS 9042	B. Antoun, 8256
1	MS 9042	J. Foulk, 8256
1	MS 9042	W.-Y. Lu, 8256
1	MS 9042	J. Ostien, 8256
1	MS 9957	H. Jin, 8256
1	MS 0899	Technical Library, 9536 (electronic copy)

Sandia National Laboratories